

# Physical Processes Behind the Co-Evolution of Halos, Galaxies and Supermassive Black Holes in the IllustrisTNG Simulation

HAO LI  <sup>1,2</sup> YANGYAO CHEN  <sup>1,2</sup> HUIYUAN WANG  <sup>1,2</sup> AND HOUJUN MO  <sup>3</sup>

<sup>1</sup> Department of Astronomy, University of Science and Technology of China, Hefei, Anhui 230026, People's Republic of China;

<sup>2</sup> School of Astronomy and Space Science

University of Science and Technology of China, Hefei 230026, China

<sup>3</sup> Department of Astronomy

University of Massachusetts, Amherst MA 01003, USA

## ABSTRACT

We explore the co-evolution of dark matter halos, their central galaxies, and central supermassive black holes (SMBHs) using the IllustrisTNG (TNG) simulation. We find that the evolutionary histories of individual galaxies in the  $M_{\text{BH}}-M_*$  plane can be decomposed into four distinct phases, separated by three transition points. We identify the driving processes of galaxy evolution within each phase and derive the conditions necessary and sufficient for transitions to subsequent phases. The first phase is dominated by star formation, with its duration primarily determined by the mass of the SMBH seed and the surrounding gas environment. The second phase is characterized by rapid SMBH growth, and the transition to the next phase occurs when the thermal-mode feedback of active galactic nucleus (AGN) can unbind gas from the galaxy. The third phase involves self-regulation of the SMBH, and the transition to the quenched phase occurs when the kinetic-mode feedback of AGN counterbalances gas cooling within the subhalo. The final phase is dominated by mergers. We investigate the use of scaling relations among different mass components and evolutionary phases to understand processes implemented in TNG and other simulations, and discuss how current and forthcoming observations can be used to constrain models.

*Keywords:* galaxies: evolution – galaxies: active – galaxies: nuclei – galaxies: clusters: general

## 1. INTRODUCTION

Structure formation in the  $\Lambda$ CDM cosmology is predicted to follow a hierarchical paradigm (e.g. Peebles 1980; Blumenthal et al. 1984; Mo et al. 2010), in which structures grow from smaller to larger scales, forming virialized dark matter halos of larger masses. Gas associated with dark matter, which may be heated by shocks associated with gravitational collapse, can cool radiatively and contract until it becomes self-gravitating and fragments to form stars. Under extreme conditions that are most likely fulfilled in the central regions of galaxies, the gas and/or stars can be turned into black holes (BHs); the latter can continue to grow via accretion of gas and/or mergers with stars and other BHs. This may lead to the formation of supermassive black holes (SMBHs) observed in the centers of many galaxies (e.g. Kormendy & Ho 2013; Graham & Sahu 2023a; Maiolino

et al. 2024). In this scenario of structure formation, small and compact objects in the cosmic hierarchy are embedded in the environments defined by the more extended and less dense structures. Inversely, energetic processes on small scales can affect their environments through feedback processes, forming a bidirectional connection in the hierarchy. Examples of such feedback include the AGN feedback from an accreting SMBH, which can push/heat the gas within its host galaxy (e.g. Fabian 2012; Liu et al. 2013; Heckman & Best 2014; Kubo et al. 2022; Donahue & Voit 2022) and halo (e.g. Li et al. 2022; Luo et al. 2024; Liu et al. 2024), and the feedback from star formation, which can change the composition and state of the interstellar and circumgalactic medium (e.g. Fielding et al. 2017; Hopkins et al. 2020; Li et al. 2020; Deng et al. 2024) and even modify the distribution of dark matter (e.g. El-Zant et al. 2001; Mo & Mao 2004; Agertz & Kravtsov 2016; Acevedo et al. 2023; Yang et al. 2024). The formation and evolution of SMBHs, galaxies and halos are thus indispensable to one another, and have to be modeled together in order to understand the physical processes behind observational phenomena.

Corresponding author: Hao Li, Yangyao Chen, Huiyuan Wang  
lh123@mail.ustc.edu.cn, yangyaochen.astro@foxmail.com, whywang@ustc.edu.cn

Numerous theoretical efforts have been made to model structure formation in the current cosmological framework. Numerical (e.g. Schaye et al. 2015; Hopkins et al. 2018; Davé et al. 2019; Pillepich et al. 2018a; Blank et al. 2019), semi-analytical (e.g. White & Rees 1978; Somerville et al. 2008; Henriques et al. 2015; Croton et al. 2016; Baugh et al. 2019), analytical (e.g. Mo et al. 1998; Hernquist & Springel 2003; Sharma & Theuns 2020; Bower et al. 2017; Dekel et al. 2023) and empirical (e.g. Zheng et al. 2005; Hearin et al. 2016; Xu et al. 2018; Mo et al. 2024; Chen et al. 2024a,b) models have been developed to describe the physical processes on different scales and to discover, test and verify the assumptions and prescriptions governing these processes. Various observations of SMBHs, galaxies and halos have been used to constrain these models. Examples of observations include the spatially resolved properties of individual galaxies and clusters (e.g. Lin et al. 2019; Fahrion et al. 2020; Jing & Li 2024); the spatial number density of galaxies binned by different quantities, such as the galaxy luminosity or stellar mass function, and AGN luminosity or SMBH mass function (e.g. Chen et al. 2019; Padmanabhan & Loeb 2023; Wang et al. 2024a); the spatial correlation of galaxies and AGNs (e.g. Li et al. 2006; García-Bernete et al. 2024; Saxena et al. 2024); the joint distribution or scaling relations between different quantities, such as the SMBH mass-stellar mass relation (e.g. Kormendy & Ho 2013; Graham & Sahu 2023a; Hong et al. 2023), the SMBH mass-halo mass relation (e.g. Zhang et al. 2024; Li et al. 2024a), and the stellar mass-halo mass relation (e.g. Yang et al. 2007, 2008; Moster et al. 2010; Wechsler & Tinker 2018; Zhang et al. 2022).

Comparisons between observations and models have led to many important conclusions about the physical processes on different scales and the interaction between them. For example, the star formation efficiency, defined as the ratio of stellar mass to halo mass, is found observationally to be an unimodal function of halo mass, peaked at around a halo mass of  $M_{h,c} \approx 10^{12} M_\odot$  (e.g. Yang et al. 2003, 2012; Behroozi et al. 2013). The peak star formation efficiency is about a few percent, much lower than the value of  $\approx 0.16$  allowed by the cosmic baryon fraction. Two different channels of feedback, one from stars (e.g. Kauffmann & Charlot 1998; Hopkins et al. 2012, 2014; Anglés-Alcázar et al. 2017; Hopkins et al. 2021) and the other from AGNs (e.g. Bower et al. 2017; Weinberger et al. 2018; Davé et al. 2019) are thus proposed to suppress the star formation, and are inferred to be dominant at low- and high-masses, respectively. Another example is the relation between SMBH mass and galaxy bulge/total stellar mass, which is observed to roughly follow a power law (e.g. Kormendy & Ho 2013; Graham & Sahu 2023a,b; Hong et al. 2023). Different mechanisms, such as star formation and SMBH growth regulated by AGN feedback (e.g. Di Matteo et al. 2005; Weinberger et al. 2018; Hong et al. 2023),

and the galaxy-galaxy and SMBH-SMBH mergers (e.g. Peng 2007), have been proposed to explain the relation, in particular the power-law index. Precise measurements of the relation over a wide range of redshift from observations are thus critical to distinguish theoretical models, although such measurements are difficult to make at high redshifts (e.g. Schaye et al. 2010; Kormendy & Ho 2013; Greene et al. 2020). The stellar mass-halo mass relation and the SMBH mass-stellar mass relation also imply a correlation in mass between SMBHs and halos, as indeed found observationally by using halo masses obtained from the abundance matching (Behroozi et al. 2019), satellite kinematics (Ferrarese 2002), gravitational lensing (Zhang et al. 2024; Li et al. 2024a), and luminosity in X-ray (e.g. Gaspari et al. 2019; Voit et al. 2024), and SMBH mass from velocity dispersion (e.g. Zahid et al. 2016, 2018; Sohn et al. 2020; Shankar et al. 2020). Although the correlation between SMBH mass and halo mass may be just a phenomenological coincidence, physical frameworks involving the synergy between halo potential and AGN feedback in regulating the baryon cycle from SMBH scales to halo scales have been proposed to interpret the correlation (e.g. Bower et al. 2017; Voit et al. 2024), and observational evidences supporting the interpretation have been identified (e.g. Bandara et al. 2009; Bogdán & Goulding 2015; Zhang et al. 2024).

James Webb Space Telescope (JWST) has opened a new era to study galaxy formation at high redshift. Over the past two years, observations with JWST have discovered a large number of galaxies that are much different from those seen in the local Universe. Galaxies at high redshift appear to be more irregular and clumpy (e.g. Ma et al. 2018; Kuhn et al. 2024; Hirano & Yoshida 2024; Bik et al. 2024), with some dominated by dense star-forming clumps (e.g. Mowla et al. 2024; Adamo et al. 2024). As the coupling of feedback energy from accreting SMBHs is expected to largely depend on the morphology (Sivasankaran et al. 2025) and clumpiness (Dutta et al. 2024) of the host galaxy, SMBHs at high redshift may follow the relations with their host galaxies and halos that are different from those in the local Universe. Meanwhile, an abundant population of “little red dots” (LRDs), featured by reddened spectra and small sizes, has been discovered at  $z \gtrsim 4$ , and has been inferred as AGNs and/or young stars obscured by dust (Matthee et al. 2024; Pérez-González et al. 2024; Li et al. 2024b). If LRDs are indeed AGNs, this population of SMBHs is likely to reside in galaxies in a special stage of the evolution, and extends our observational picture of actively accreting SMBHs to the range of low BH mass in the early Universe. In addition, a recent analysis by Wang et al. (2024b) targeting at a young galaxy at  $z \approx 8$  has suggested that its emission lines and spectral slope are most consistent with a cluster of Pop-III stars. The massive stars within this cluster are thus candidates for SMBH seeds. The above observations with JWST qual-

itatively support the theoretical expectations of galaxy formation in the  $\Lambda$ CDM paradigm, and, for the first time, join the pieces of information throughout the full growth histories of galaxies and SMBHs from their infancies to the present day. To use such observations to constrain theoretical models, it is crucial to identify processes that are responsible for salient observational properties, and to understand how different processes are linked together to produce the populations of galaxies and SMBHs observed at any given time.

In this paper, we use the hydrodynamical simulation, IllustrisTNG, to study the co-evolution of SMBHs, galaxies and halos. We quantify the growth histories of individual systems, break each history into a series of distinct phases by a set of transition points, and identify the driving processes of each phase. The results found in this paper are specific to IllustrisTNG, but the method can be applied to other theoretical models as a unified way to compare models with each other and with observations.

This paper is organized as follows. In §2, we introduce the simulation data and sample. In §3, we define the phases and transitions. In §4, we analyze the co-evolution of SMBHs, galaxies and halos in each phase, identify the driving processes, and derive the conditions for the transition to the next phase. In §5, we discuss the potential use of observations to constrain the models. In §6, we summarize our results.

## 2. DATA AND SAMPLES

In this paper, we use data from the IllustrisTNG project (Marinacci et al. 2018; Naiman et al. 2018; Nelson et al. 2018; Pillepich et al. 2018a; Springel et al. 2018; Nelson et al. 2019) to investigate the co-evolution of dark matter halos, galaxies, and supermassive black holes (SMBHs). The physical and subgrid models adopted by IllustrisTNG are detailed in the method papers of the project (Weinberger et al. 2017; Pillepich et al. 2018b) together with specific improvements over the original Illustris simulation (Vogelsberger et al. 2013; Genel et al. 2014; Sijacki et al. 2015).

To achieve a balance between sample size and numerical resolution, we use the IllustrisTNG100-1 run (hereafter TNG), which has a simulation box of  $\approx 110.7$  comoving Mpc on each side. Galaxy formation in the box is simulated with  $2 \times 1820^3$  baryon elements, with a mass resolution of  $m_{\text{baryon}} = 1.4 \times 10^6 M_{\odot}$ . TNG adopted a flat  $\Lambda$ CDM cosmology, with parameters taken from the Planck2015 results (Planck Collaboration et al. 2016):  $h = H_0/(100 \text{ km/s/Mpc}) = 0.6774$ ,  $\Omega_{\text{M},0} = 0.3089$ ,  $\Omega_{\text{B},0} = 0.0486$ , and  $\Omega_{\Lambda,0} = 0.6911$ .

Groups and galaxies are identified from the simulation, and information about individual halos and galaxies is provided. Dark matter halos are selected using the friends-of-friends (FoF) algorithm with a linking length  $b = 0.2$  (in units of the mean separation of dark matter particles). Dark matter subhalos are identified us-

ing the SUBFIND algorithm (e.g. Springel et al. 2001; Rodriguez-Gomez et al. 2015) to connect all of the gravitationally bound particles or cells. Baryon particles are linked to the same group as their closest dark matter particles, and galaxies are defined as the baryon components of subhalos in FoF-groups. Typically albeit not always (e.g. Nelson et al. 2019), the most massive subhalo within a halo is defined as the central subhalo, and the galaxy associated with it is referred to as the central galaxy. All subhalos other than the central within a halo are “satellites”. Throughout this paper, we only consider subhalos of a cosmological origin defined by the SubhaloFlag, as described in the data release of TNG (Nelson et al. 2019).

A baryonic version of the SUBLINK algorithm is applied to TNG to build the subhalo merger trees (see Rodriguez-Gomez et al. 2015, for details). Each subhalo is linked with a set of progenitor subhalos, among which the one with the “most massive history” is defined as the first/main progenitor. To trace the evolution of a halo, its central galaxy, and the central SMBH within the central galaxy, we follow the main progenitor of the central subhalo recursively back in time. This extracts a branch of subhalos from the whole merger tree rooted in the subhalo in consideration, and we refer to it as the main branch of this root subhalo/galaxy/SMBH.

TNG has provided a list of available properties for each halo, subhalo, galaxy and SMBH (see Nelson et al. 2019). For other properties required by this study but not provided in the data release, we compute them from the particles/gas cells. The properties used in the paper are listed as follows.

- $M_{\text{h}}$ : halo mass, defined as the total mass enclosed in a sphere centered on the particle of minimal gravitational potential among all particles in the FoF halo, with a radius,  $R_{\text{h}}$ , defined so that the mean density within the sphere is 200 times the mean density of the universe at the epoch when the halo is identified. The circular velocity of the halo at  $R_{\text{h}}$  is defined as the virial velocity  $V_{\text{h}}$ .
- $M_{*}$ : stellar mass of the galaxy, defined as the sum of the masses of the bound stellar particles enclosed in a sphere centered on the particle with minimum gravitational potential among all particles within the subhalo, with a radius equal to  $2R_{*,1/2}$ , twice of the stellar half-mass radius of the galaxy.
- $M_{\text{BH}}$ : the mass of the most massive black-hole particle in the subhalo.
- $M_{\text{gas}}(< R)$ : the sum of masses of all bound gas cells enclosed in a sphere centered on the same location as that for  $M_{*}$ , with a radius  $R$ .
- $V_{\text{max}}$ : the maximum of the spherically-averaged rotation curve, accounting for the gravity of all species of particles/cells.

- $\dot{M}(t_n)$ : the growth rate of mass  $M$  at the  $n$ -th snapshot, estimated by central difference as

$$\dot{M}(t_n) = \frac{M(t_{n+1}) - M(t_{n-1})}{t_{n+1} - t_{n-1}}, \quad (1)$$

where  $t_{n-1}$ ,  $t_n$  and  $t_{n+1}$  are the cosmic times of the previous, current, and next snapshots.

- $\dot{M}(t_n)/M(t_n)$ : the specific growth rate of mass  $M$  at the  $n$ -th snapshot.

For the halo, stellar and SMBH masses, the definition of  $\dot{M}(t_n)$  yields the halo accretion rate (HAR), the star formation rate (SFR), and the black hole accretion rate (BHAR), respectively, and the definition of  $\dot{M}(t_n)/M(t_n)$  yields their specific values: the specific halo accretion rate (sHAR), the specific black hole accretion rate (sBHAR), and the specific star formation rate (sSFR). Note that the integration of the growth rate defined here is ensured to be equal to the mass whose evolution pattern is the main focus of this paper.

To tell whether a galaxy is star-forming or quenched, we find its instantaneous star formation rate by summing over all gas cells within  $2R_{*,1/2}$ , and obtain the instantaneous sSFR by dividing the instantaneous SFR by  $M_*$ . We note that the instantaneous SFR is noisy due to the stochastic nature of the subgrid models, the finite resolution of the simulation and the defects of the structure finder algorithms that link the resolution elements. Some galaxies, in particular the high-redshift ones, can thus have sudden drops in sSFR in some individual snapshots, make an excursion to the “quenched” state and return to the “star-forming” status later. To mitigate the noise, we smooth the instantaneous sSFR along the main branch of the subhalo merger tree by a running Gaussian kernel with standard deviation equal to the dynamical timescale ( $t_{\text{dyn},h} \equiv R_h/V_h$ ) of the host halo at each snapshot. We define a galaxy to be quiescent/quenched if the sSFR so obtained is less than the threshold of  $10^{-11} \text{ yr}^{-1}$ , which is commonly used in literatures (e.g. Schaye et al. 2015; Cui et al. 2021; Habouzit et al. 2021; Bluck et al. 2024). For each quenched galaxy, we identify its quenching time,  $t_q$ , as the first time when its smoothed instantaneous sSFR falls below the threshold of  $10^{-11} \text{ yr}^{-1}$ .

Fig. 1 shows the main-branch histories of individual galaxies in the  $M_{\text{BH}}-M_*$  plane. The top panel plots the histories of galaxies randomly selected from all central galaxies with  $M_* > 10^{8.5} M_\odot$  at  $z = 0$ , 10 for star-forming (blue) and 10 for quenched (red). Here, for each history,  $M_*$  and  $M_{\text{BH}}$  are scaled by their values at a reference redshift when  $M_{\text{BH}}/M_*$  reaches its minimum. For each history, the  $M_{\text{BH}}-M_*$  curve presents regular patterns that mark the different phases undergone by the galaxy. In the early time before the reference point, the curve is quite flat, indicating that the growth of SMBH is slower than that of the stellar component. A sharp transition appears at about the reference point, followed by a rapid growth of SMBH. In the later time,

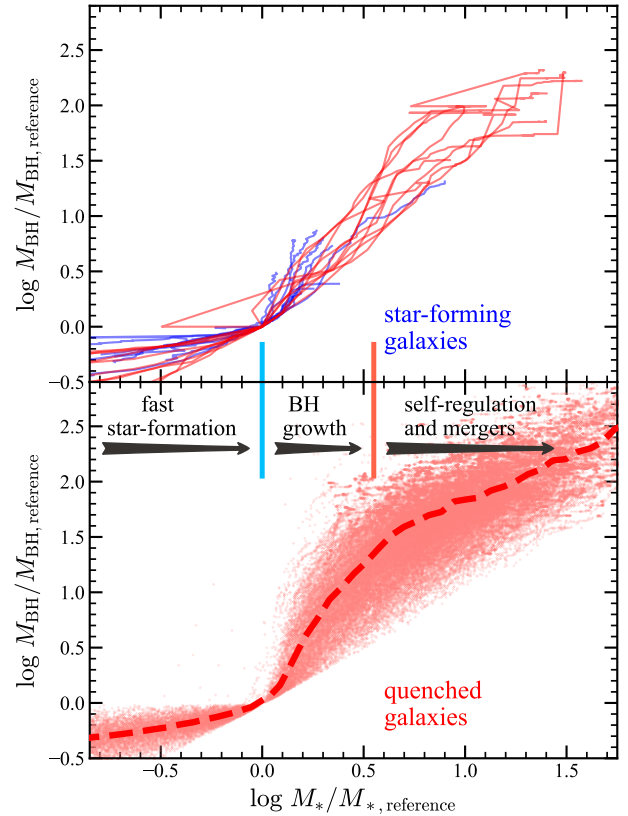


**Figure 1.** The main-branch histories of individual galaxies in the  $M_{\text{BH}}-M_*$  plane. For each branch,  $M_*$  and  $M_{\text{BH}}$  are scaled by their values at a reference redshift when the ratio,  $M_{\text{BH}}/M_*$ , reaches its minimum. **Top panel** shows the histories of randomly selected galaxies in TNG at  $z = 0$  with  $M_* > 10^{8.5} M_\odot$ , 10 for star-forming (blue) and 10 for quenched (red). **Bottom panel** shows the sample of quenched galaxies used in the analysis throughout this paper. Here, each red dot represents a galaxy at a snapshot in a main branch. The red dashed curve shows the median among all branches. See §2 for the details of sample and selection.

the difference between star-forming and quenched galaxies appears. For quenched galaxies, the growth of  $M_{\text{BH}}$  slows down, and eventually reaches a regime where significant “jumps” appear in both  $M_*$  and  $M_{\text{BH}}$ . For most star-forming galaxies, this later phase is missing.

Much of the effort in this paper is to quantify the distinct phases and identify the underlying mechanisms driving the evolution during each phase and the transition to the next. In this paper, the main branches to be analyzed are selected according to the following criteria:

- (i) The root subhalo is a central subhalo at  $z = 0$ .
- (ii) The root subhalo has  $M_h \geq 5 \times 10^{11} M_\odot$ ,  $M_* \geq 10^9 M_\odot$ , and has a SMBH in it.
- (iii) The root galaxy is quenched.

- (iv) The branch can be traced up to snapshot 10 ( $z \approx 7$ ). The histories of subhalos before this redshift are not used.
- (v) The branch does not contain a “backsplashed” subhalo that temporarily falls into another halo, becomes a satellite, and returns to being central after its halo mass exceeds one-third of the halo mass at  $z = 0$ .

The requirement for the subhalo to be a central (criterion i) and to have never been a satellite (criterion v) is to avoid the effect of the environment which provides additional channels to quench the galaxy (see, e.g. [Kauffmann et al. 2013](#); [Ayromlou et al. 2023](#); [Wang et al. 2023](#)). The lower limit imposed on  $M_*$  (criterion ii) ensures that the root subhalo has at least  $\approx 1000$  stellar particles, thus alleviating the artifacts due to numerical resolution. The requirement of the complete history (criterion iv) and quenched state (criterion iii) ensures that none of the four phases (see §3) is missed in the history, which simplifies the analysis and presentation of this paper. The numbers of galaxies passing the above 5 criteria are 6291208, 8280, 1682, 1594 and 1429, respectively. In addition, we have excluded two galaxies that cannot be properly fitted by the function to be discussed in §3. The conclusions of this paper thus apply only to quenched galaxies at  $z = 0$ , for which we have checked that the above selection criteria do not lead to significant bias. For star-forming galaxies, as shown in the top panel of Fig. 1, their histories appear similar to the quenched galaxies with some later phases truncated. Whether or not this similarity is quantitatively true, how the evolution of star-forming galaxies in each phase and at each transition is different from that of quenched galaxies, and how SMBH feedback acts differently between star-forming and quenched galaxies (e.g. [Fabian 2012](#); [Dubois et al. 2015](#); [Weinberger et al. 2018](#)), remain to be open questions to be addressed further.

The lower panel of Fig. 1 shows the main-branch histories in the  $M_{\text{BH}}-M_*$  plane for all the galaxies selected in our sample. The dashed red curve shows the median among all the histories. We label the processes that drive the evolution of galaxies in different phases in this figure, and we will discuss them in detail in the following sections.

### 3. EVOLUTIONARY PHASES AND TRANSITIONS

The similarity of the trajectories of the quiescent galaxies in Fig. 1 indicates that a universal function can be used to fit the evolution path of each quiescent galaxy in the  $M_{\text{BH}}-M_*$  plane. To quantify the transitions and phases in the growth histories, we fit all snapshots before the quenching time,  $t_{\text{q}}$ , by the following piecewise continuous function:

$$y(x) = \begin{cases} \frac{(a+b)^3}{2} \left[ \frac{1}{(x-x_0-a)^2} - \frac{1}{a^2} \right] + y_0, & \text{if } 0 \leq x < x_0; \\ k(x - x_0) + y_0, & \text{if } x \geq x_0, \end{cases} \quad (2)$$

where  $y = \log(M_{\text{BH}}/\text{M}_\odot)$ ,  $x = \log(M_*/\text{M}_\odot)$ , and  $(x_0, y_0, k, a, b)$  are the five free parameters characterizing the evolutionary phases and transitions. The values of the free-parameters are obtained by minimizing the loss function,  $\chi^2 = \sum_s (y_{\text{sim},s} - y_s)^2$ , computed using the simulated value ( $y_{\text{sim}}$ ) and the value predicted by the fitting function ( $y$ ) at every snapshot,  $s$ . The optimization is performed using the Levenberg-Marquardt algorithm, which is designed for solving non-linear least squares problems. By design, the fitting function explicitly includes three transition points at which the behavior of the galaxy in the  $M_{\text{BH}}-M_*$  plane changes significantly. The first transition point is  $x = x_0 - b$  at which  $dy/dx = 1$ . This marks the time when the growth of the SMBH begins to outpace the star formation. The second transition is at  $x = x_0$ , where the rapid growth in the SMBH mass ends. Given that TNG adopts a Bondi accretion upper-bound only by the Eddington limit, the growth of SMBH during  $x_0 - b < x < x_0$  can be very fast. This behavior can be captured by a value of  $a$  close to zero. For  $x \geq x_0$ , the function  $y(x)$  is designed to be linear, describing a power-law relation,  $M_{\text{BH}} \propto M_*^k$ . The final transition is the ending point of the domain of the fitting function, which, by design, is the quenching point of the galaxy. The red dashed curve shows the best-fit function for an example galaxy in the left panel of Fig. 2, with three black hexagons marking the three transition points (see below for the notations), respectively. The fitting captures well all the nonlinear features of the simulated points in this example. Since mergers do not dominate the growth of  $M_{\text{BH}}$  and  $M_*$  compared with the accretion of gas and in-situ star formation before quenching (see e.g. figure 7 of [Weinberger et al. 2018](#)), the nuances introduced by mergers in the growth of galaxies in the  $M_{\text{BH}}-M_*$  plane do not significantly affect the fitting. For reference, in Appendix A, we quantify the goodness-of-fit for all galaxies in our sample. For most galaxies in our sample, the root-mean-square error is less than 0.1 dex, and the maximum absolute error is less than 0.3 dex, indicating that the fittings are reliable for individual galaxies. In addition, we have performed tests by tweaking the fitting function and resampling the data points used in the fitting, and found that the identification of the transition points is robust against such changes.

The three transition points break the evolution of a galaxy into four phases. According to the physical processes to be introduced in §4, we name these phases as follows:

- *Phase-1: Star-formation dominated growth.* This phase is characterized by a slow growth of the SMBH, with  $M_{\text{BH}}$  remaining close to the seeded mass, and a significant growth of  $M_*$  due to active star formation.
- *Phase-2: SMBH-accretion dominated growth.* This phase is featured by a rapid growth in  $M_{\text{BH}}$ , by up to

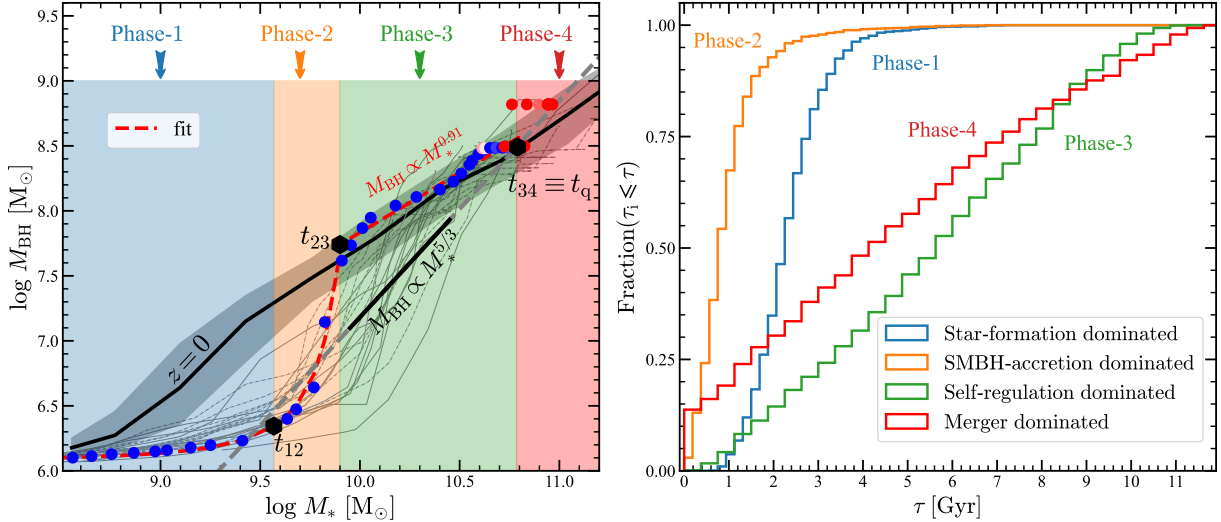


**Figure 2.** The phases and transitions in the evolution histories of galaxies. **Left panel** shows the  $M_{\text{BH}}-M_*$  histories of galaxies. **Grey curves** represent the simulated histories of 20 individual galaxies randomly selected from our sample (see §2). Dots are the history of an example galaxy, colored blue (red) if it is star-forming (quenched) at a snapshot. **Red dashed curve** shows the analytical fitting of the history for this example. Four phases are defined according to the fitting function and are labeled at the top of the panel. Three time points,  $t_{12}$ ,  $t_{23}$  and  $t_{34} \equiv t_{\text{q}}$ , are used to separate these phases (see §3 for the fitting method and the definition of phases and transitions). **Black curve** shows the median  $M_{\text{BH}}-M_*$  relation at  $z = 0$  computed using all galaxies in our sample, with the shaded area indicating the 16<sup>th</sup>–84<sup>th</sup> percentiles. **Short black line** indicates a power law,  $M_{\text{BH}} \propto M_*^{5/3}$ , to which the regulation of thermal-mode AGN feedback in Phase-3 tends to drive the galaxy (see §4.3). **Right panel** shows the cumulative distribution of  $\tau_i$ , the duration of Phase- $i$ .

two orders of magnitude, and a modest growth in  $M_*$ , by a factor of about two to three.

- **Phase-3: Self-regulation dominated growth.** This is a period during which the masses of the SMBH and the stellar component grow at a comparable rate in logarithmic scales. This causes the galaxy to evolve towards a scaling relation of  $M_{\text{BH}} \sim M_*^{5/3}$  (indicated by the black short line in the left panel of Fig. 2) if it initially deviates from this relation.
- **Phase-4: Merger dominated growth.** This phase is characterized by the cease of in-situ star formation and SMBH growth. Consequently, the trajectory of a galaxy in the  $M_{\text{BH}}-M_*$  plane is stuck at around a point near the scaling relation at  $z = 0$ , with some occasional “jumps” due to mergers.

For convenience, we denote the duration of Phase- $i$  by  $\tau_i$ , and the time point of the transition from Phase- $i$  to Phase- $j$  by  $t_{ij}$ .  $\tau_1$  is defined to be the duration between  $t_{\text{seed}}$ , the time when the SMBH is seeded, and  $t_{12}$ .  $\tau_4$  is defined to be the duration between  $t_{34}$  and  $z = 0$ . For example, a galaxy stays in Phase-3 for a period of  $\tau_3$ , transits at the time  $t_{34}$  to Phase-4 and stays there for a period of  $\tau_4$ . The last transition point,  $t_{34}$ , is defined to be the quenching time of the galaxy, and thus we use  $t_{\text{q}}$  for it interchangeably.

The right panel of Fig. 2 shows the cumulative distribution of the duration for each of the four phases. Phase-1 is short for most galaxies. Phase-2 is even

shorter due to the fast SMBH growth modeled by Bondi accretion, with  $\approx 70\%$  galaxies staying there for  $\lesssim 1$  Gyr. The last two phases have nearly uniform distributions of  $\tau$  (seen from the nearly linear cumulative distributions), indicating that the quenching of a galaxy in TNG can happen at any time after the phase of rapid growth of SMBH.

#### 4. PROCESSES DRIVING THE EVOLUTION

In order to identify the underlying physical processes governing the distinct phases found phenomenologically by the curve fitting shown above, here we examine some physical properties in more detail, quantify their relations, demonstrate the conditions for their transitions, and discuss when and how they lead to the migration of a galaxy from one phase to the next.

##### 4.1. Phase-1: Star-formation dominated growth

The growth of a galaxy in the first phase is featured by a small mass of the SMBH. In TNG, a seed of SMBH with a mass of  $M_{\text{BH}} = 1.18 \times 10^6 M_{\odot}$  is placed into a galaxy when the mass of its host halo exceeds  $7.38 \times 10^{10} M_{\odot}$  (Weinberger et al. 2018). The subsequent growth of the SMBH is modeled by the Bondi-Hoyle accretion (Weinberger et al. 2017, thereafter Bondi accretion). As the accretion rate of the SMBH modeled in this way scales as  $M_{\text{BH}}^2$ , the seed thus determines the initial sBHAR. In TNG, the seed mass is small enough so that the sBHAR is initially negligible, which, together

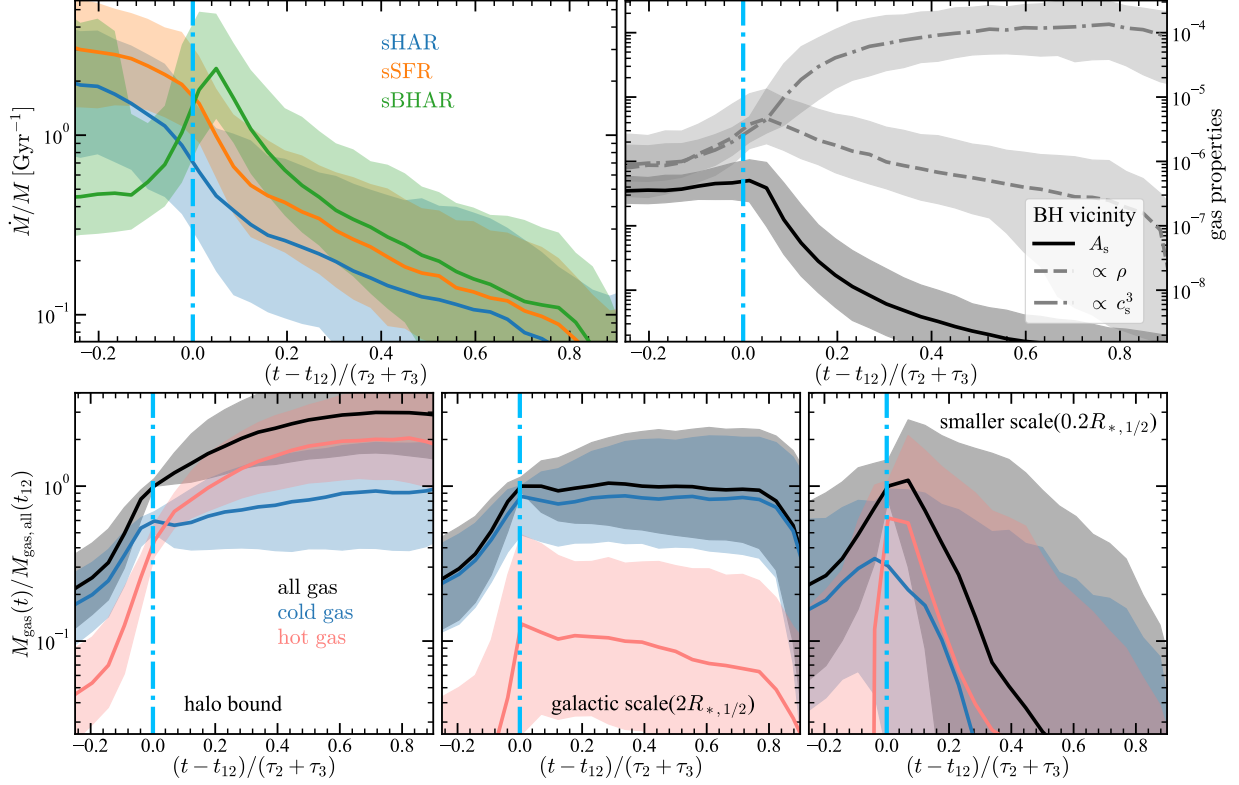


**Figure 3.** Evolutionary history of various properties around the transition point  $t_{12}$ . Each property describing the history is averaged over our sample (see §2) and shown as a function of time, measured with respect to  $t_{12}$  and scaled by the duration  $\tau_2 + \tau_3$ . The shaded area around each curve shows the 16<sup>th</sup>–84<sup>th</sup> percentiles. Each panel shows a set of related properties. **Top left** panel shows the specific growth rates of of  $M_h$  (blue),  $M_*$  (orange) and  $M_{\text{BH}}$  (green). **Top right** panel shows the gas properties involved in the definition of Bondi accretion rate (see Eq. 3 and 4) in the vicinity of the central SMBH. Three **bottom panels** show the gas masses defined at different scales: bound to the subhalo (**left**), within  $2R_{*,1/2}$  (**middle**), and within  $0.2R_{*,1/2}$  (**right**). Total, cold ( $\leq 10^5$  K), and hot ( $> 10^5$  K) gas masses are shown by black, blue and red curves, respectively, all scaled by total gas mass at  $t_{12}$ .

with a high sSFR at high redshift (e.g. Habouzit et al. 2021, see their figure 4), drives a horizontal trajectory in the  $M_{\text{BH}}-M_*$  plane for the galaxy (see the left panel of Fig. 2). The low accretion rate of SMBH also implies that its feedback effect is small, and thus the star formation in the galaxy is regulated only by the stellar feedback. A comparison of the energy release rates via different feedback channels by Weinberger et al. (2018, see their figure 1) indeed shows the domination of stellar feedback in the early time. The first phase is thus referred to as the star-formation dominated phase in this paper.

The top left panel of Fig. 3 shows the specific growth rate of different masses ( $M_h$ ,  $M_*$  and  $M_{\text{BH}}$ ) as a function of time. Each rate is averaged over the sample defined in §2. To see the growth of the whole sample during the early phases, the time is measured with respect to  $t_{12}$ , the ending point of Phase-1, and scaled by  $\tau_2 + \tau_3$ , the total time of the following two phases. The exclusion of  $\tau_1$  from the scaling factor is to avoid the ambiguity caused by the seeding time, and the inclusion of  $\tau_3$  accounts for the fact that  $\tau_2$  is too short. During

Phase-1, the sSFR follows the sHAR tightly, indicating that the formation of the stellar contents is driven by the gas accretion along with the halo growth and that the  $M_*-M_h$  relation has been well established before the seeding of SMBH. The sBHAR is significantly lower compared to the rates of the halo and galaxy, indicating that the early SMBH growth can deviate from the  $M_{\text{BH}}-M_*$  relation at  $z \approx 0$  in both TNG and observations (e.g. Kormendy & Ho 2013; Greene et al. 2020; Graham & Sahu 2023a,b; Habouzit et al. 2021; Zhuang & Ho 2023). Thus, the growth of SMBH in Phase-1 has to be understood by combining the established environment of the galaxy and the halo, and the specific strategy in the seeding of SMBH.

To quantify the growth of SMBH in Phase-1, we formulate the Bondi accretion rate as

$$\dot{M}_{\text{BH}} = A_s M_{\text{BH}}^2, \quad (3)$$

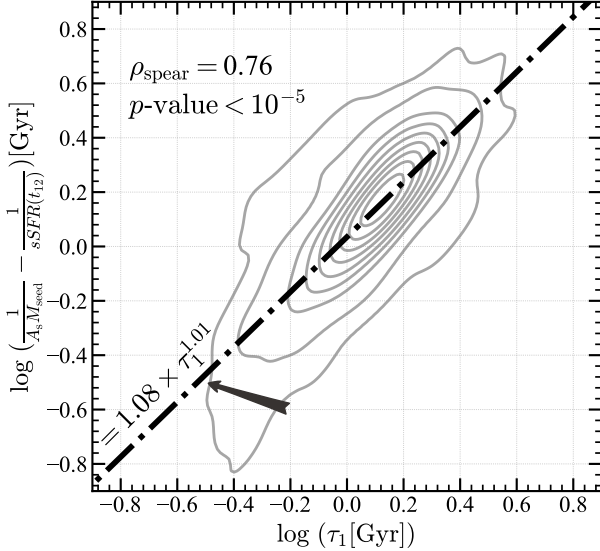


**Figure 4.** Relation between the estimated value and the simulated value of the Phase-1 duration ( $\tau_1$ ). **Grey curves**, from inner to outer, are contours enclosing 10% – 95% of the sample. **Dashed line** is a power-law fitting (in linear scale) of the relation. The normalization and power index are both close to 1, indicating that the estimated value well approximates the simulated value. See §4.1 for the details.

where the normalization factor

$$A_s \equiv \frac{4\pi G^2 \rho_{\text{gas}}}{c_s^3} = \left( \frac{1}{1.4 \text{ Gyr}} \right) \times \left( \frac{c_s}{10 \text{ km s}^{-1}} \right)^{-3} \left( \frac{n_{\text{gas}}}{0.1 \text{ cm}^{-3}} \right) \left( \frac{1}{10^6 M_{\odot}} \right), \quad (4)$$

$\rho_{\text{gas}}$  and  $c_s$  are the gas density and effective sound speed, respectively, within a smoothing kernel around the SMBH,  $n_{\text{gas}}$  is the number density of gas molecules, assuming a mean molecular weight of  $\mu = 1.2$ . Thus,  $A_s$  depends only on the gas environment around the SMBH and, by construction, is a function of the specific entropy, which is shaped by the dissipation and heating processes. The bottom three panels of Fig. 3 show the evolution of gas mass within different spatial extents. The total mass, and those in hot and cold phases, are shown by curves with different colors. Within  $2R_{*,1/2}$ , cold gas dominates the total gas mass during Phase-1, suggesting that supernova feedback alone cannot quench the star formation. This is consistent with the cooling rate of non-star-forming cells computed by Weinberger et al. (2018, see their figure 1), which always balances the energy output from stellar feedback in the early time. In the innermost region ( $r \lesssim 0.2R_{*,1/2}$ ) during Phase-1, the cold component also dominates the gas mass, which, together with the high gas density in this region (e.g. Bower et al. 2017), implies that the early growth of SMBH is fed mainly by star-forming gas. The quantitative state of star-forming gas cells, however, de-

pends on the subgrid recipes assumed by TNG, which cannot be estimated analytically. We therefore directly compute the state variables from the simulation data. The gas density,  $\rho_{\text{gas}}$ , is averaged by an SPH kernel (e.g. Weinberger et al. 2017) over a sphere centered on the SMBH and enclosing approximately 256 cells (defined by the radius  $\text{BH\_Hsm1}$  in the particle data of TNG). The effective sound speed,  $c_s$ , which includes the contribution from the Alfvén speed of the magnetic field, is obtained by inserting Eq. (3) using the values of  $\rho_{\text{gas}}$  estimated as above, and  $M_{\text{BH}}$  and  $\dot{M}_{\text{BH}}$  read from the simulation data. The evolutions of  $A_s$ ,  $\rho_{\text{gas}}$  and  $c_s$  are shown in the top right panel of Fig. 3. An interesting fact is the constant value of  $A_s$  during Phase-1, which implies that the gas processes around the SMBH are effectively adiabatic. We note that this is an outcome of the specific choice of TNG on the effective equation of state (eEOS) for star-forming cells and the subgrid model for the magnetic field (e.g. Springel & Hernquist 2003; Vogelsberger et al. 2013; Pillepich et al. 2018b).

Using the fact that  $A_s$  is roughly constant in Phase-1, we integrate Eq. (3) and obtain

$$\frac{M_{\text{BH}}(t)}{M_{\text{seed}}} = \frac{1}{1 - A_s M_{\text{seed}} \cdot (t - t_{\text{seed}})}, \quad (5)$$

where  $M_{\text{seed}} \equiv M_{\text{BH}}(t_{\text{seed}})$ . This solution becomes divergent at  $t - t_{\text{seed}} = (A_s M_{\text{seed}})^{-1}$ , which sets the upper limit of  $\tau_1$ . By our definition, the ending point of Phase-1 is when sBHAR equals sSFR. Substituting this definition into Eqs. (3) and (5), we obtain the duration of Phase-1 as

$$\tau_1 = \frac{1}{A_s M_{\text{seed}}} - \frac{1}{\text{sSFR}} \leq \frac{1}{A_s M_{\text{seed}}}. \quad (6)$$

This result implies that, the duration of the phase when star formation outpaces SMBH growth is determined by (i) the seeding strategy of SMBH in the simulation, or the formation of SMBH seed in the real Universe; (ii) the specific entropy of gas surrounding the SMBH seed, namely, the boundary conditions provided by halo accretion, star formation and stellar feedback; (iii) the definition of the end of the phase. The upper limit of  $\tau_1$ ,  $(A_s M_{\text{seed}})^{-1}$ , is determined by only (i) and (ii).

Fig. 4 shows the distribution of  $\tau_1$  directly obtained from the fitting function described in §3, in comparison with the value estimated by Eq. (6). To avoid large fluctuations at a specific snapshot, we use the average  $A_s$  during Phase-1. The contour in the figure shows the distribution of SMBHs and the dot-dashed line shows a power-law fitting. The normalization and power index of the fitting are both close to 1, indicating that the estimation of  $\tau_1$  by Eq. (6) is accurate. Thus, from Eq. (6), the transition from star-formation dominated growth to SMBH-accretion dominated growth, with a given definition of the transition, is a combined consequence of the subgrid model adopted by TNG: the low-mass seeds,

the Bondi accretion rate, and the eEOS of star-forming gas.

A critical task in hydrodynamical simulations is to implement different recipes of SMBH seeding and growth, to embed SMBHs in different environments, and to understand their observational consequences. For example, [Bower et al. \(2017\)](#) analytically estimated the condition for the triggering of rapid SMBH growth (the transition at  $t_{12}$  in our terminology), and tested it in the EAGLE simulation with a list of model variants. As EAGLE is different from TNG in its hydrodynamic solver and the thermal-mode stellar feedback, the results and the interpretations can be different. Indeed, their results suggested that the transition at  $t_{12}$  is caused by the transition of the effect of stellar feedback, which is initially effective in expelling gas from the galaxy by the buoyant outflow, but then becomes ineffective when the halo grows massive and the gas environment of the galaxy becomes hot. The transition is thus controlled by a critical halo mass, which is suggested to be  $\sim 10^{12} M_\odot$  and depend moderately on redshift. A follow-up study by [McAlpine et al. \(2018\)](#) based on EAGLE instead suggested that the transition occurs at a nearly constant virial temperature of  $\approx 10^{5.6}$  K. Other works also suggested that active star formation can expel gas from the vicinity of the central SMBH, reduce the gas density and suppress the accretion of the SMBH (e.g. [Habouzit et al. 2017](#); [Anglés-Alcázar et al. 2017](#); [Hopkins et al. 2021](#); [McAlpine et al. 2018](#); [Byrne et al. 2023](#)). These models thus create environments for the growth of SMBH in the star-formation dominated phase that are different from that in TNG, and are expected to produce  $\rho_{\text{gas}}(t)$  and  $c_s(t)$  curves that are different from the smooth, slowly increasing curves shown in the top right panel of Fig. 3. The evolution of  $A_s$  may also be changed, which can lead to an evolution equation of  $M_{\text{BH}}$  different from our Eq. (5).

After  $t_{12}$ , the rapid growth of the SMBH starts together with strong thermal-mode feedback. Using the estimation given by [Weinberger et al. \(2018\)](#), see their §2.4), the ratio of the energy output rate from thermal-mode AGN and star formation for the metal-enriched ( $Z \gg 0.002$ ) gas is

$$\frac{\dot{E}_{\text{AGN, thermal}}}{\dot{E}_{\text{SF}}} \approx 3 \times 10^3 \frac{\dot{M}_{\text{BH}}}{\dot{M}_*}. \quad (7)$$

Therefore, once  $M_{\text{BH}}/M_* \gtrsim 10^{-3}$ , the cumulative energy output from AGN dominates over that from star formation, and the galaxy starts to migrate from the supernova-regulated phase to the AGN-regulated phase. The example galaxy in Fig. 2 shows that  $M_{\text{BH}}/M_*$  indeed reaches this critical value at around  $t_{12}$ , thus supporting our definition of this transition point and the interpretation of it as a transition to the SMBH-accretion dominated phase.

#### 4.2. Phase-2: SMBH-accretion dominated growth

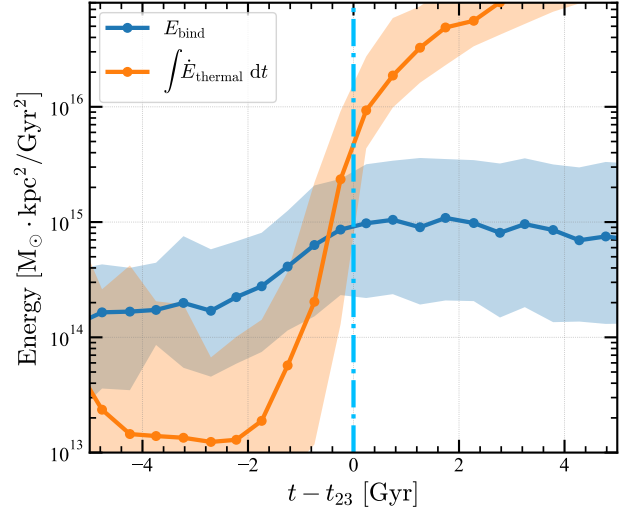


**Figure 5.** Evolution of energies at around the transition point  $t_{23}$ . **Blue curve** shows  $E_{\text{bind}}$ , the binding energy of the gas within the galaxy. **Orange curve** shows  $E_{\text{agn}}$ , the cumulative feedback energy from AGN. Both are shown as a function of time, measured with respect to  $t_{23}$ . See §4.2 for the details.

The transition point,  $t_{12}$ , by definition, is the time when the sBHAR becomes larger than the sSFR. As shown in the top left panel of Fig. 3, the sBHAR and sSFR cross each other at this point. In the  $M_{\text{BH}}-M_*$  plane, the trajectory makes a transition at  $t_{12}$  from nearly horizontal to nearly vertical, as seen from the example shown in Fig. 2. After this point, the sBHAR continues to increase, reaches a peak, and then declines to a rate comparable to the sSFR. In contrast, the sSFR always declines with time and remains below the sBHAR during Phase-2. The obvious reason for the fast growth of the SMBH in Phase-2 is the Bondi accretion implemented by TNG. For a given gas environment, the BHAR is  $\propto M_{\text{BH}}^2$ , so that

$$\frac{d \ln M_{\text{BH}}}{dt} \propto \exp(\ln M_{\text{BH}}). \quad (8)$$

Thus, the growth of SMBH in the logarithmic scale is exponential. This growth, however, can only last for a short period before the properties of the surrounding gas are changed significantly by the AGN feedback. The cumulative distribution in the right panel of Fig. 2 shows that the duration of Phase-2 is the shortest among the four phases, with a median of  $\approx 1$  Gyr.

To derive a general condition for the ending of Phase-2, we start with the equation of energy conservation for the gas within the galaxy:

$$dE_{\text{gas}} = -dE_{\text{cool}} + dE_{\text{fdbk}}, \quad (9)$$

where  $E_{\text{gas}} \equiv E_{\text{in}} + E_{\text{k}} + E_{\text{v}}$  is the total energy of the gas, defined as the sum of the internal, kinetic, and gravitational potential energies,  $E_{\text{cool}}$  is the energy loss due

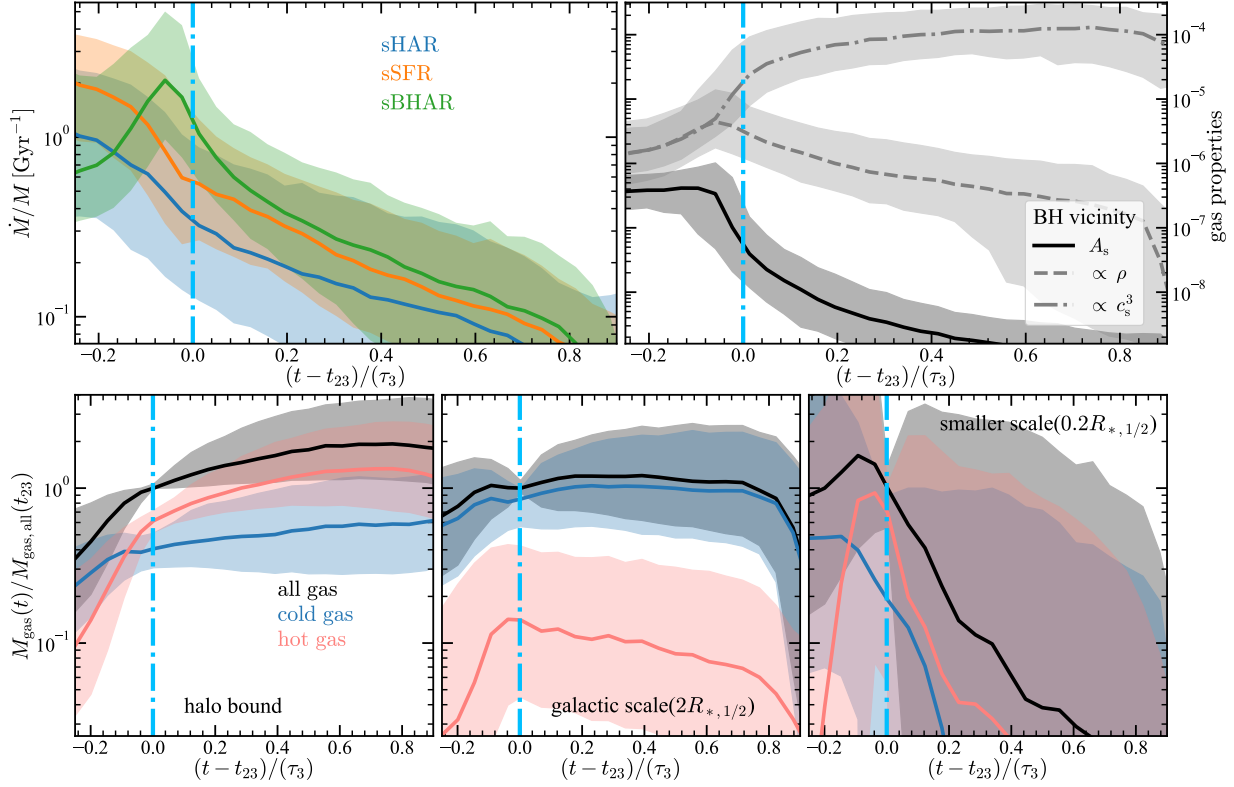


**Figure 6.** Similar to Fig. 3, but here the time is measured with respect to  $t_{23}$  and scaled by  $\tau_3$ , so that the evolution of galaxies around the transition from SMBH-accretion dominated growth to self-regulation dominated growth is clear.

to radiative cooling, and  $E_{\text{fdbk}}$  is the energy input from feedback. The ending of fast SMBH accretion requires a significant reduction in the amount of gas that can fuel the SMBH. To be achieved, the gas of the entire galaxy, in particular that in the inner region, has to be significantly affected by the feedback, because otherwise cold gas clumps that can form in the galaxy will sink into the center and fuel the SMBH. Motivated by the flat curve of the total gas mass shown in the bottom center panel of Fig. 3 after  $t_{12}$ , we express the gas mass at time  $t$  around  $t_{23}$  as

$$M_{\text{gas}}(t) - M_{\text{gas}}(t_{23}) \approx \dot{M}(t_{23})(t - t_{23}) = 0, \quad (10)$$

With this, the conservation equation (9) can be rewritten as

$$\begin{aligned} M_{\text{gas}} d\epsilon_{\text{gas}} &= -dE_{\text{cool}} + dE_{\text{fdbk}} \\ &= \eta_{\text{eff}} dE_{\text{fdbk}}, \end{aligned} \quad (11)$$

where  $\epsilon_{\text{gas}} \equiv E_{\text{gas}}/M_{\text{gas}}$  is the specific energy of gas, and  $\eta_{\text{eff}}$  is the effective fraction of the feedback energy that is coupled to the gas after subtracting radiative cooling. The time integration of the left-hand side of Eq. (11) until the gas becomes unbound is exactly the binding energy, and we use the virial theorem (e.g. Terrazas et al. 2020) to estimate it:

$$M_{\text{gas}} \int d\epsilon_{\text{gas}} = E_{\text{bind}} \approx \frac{1}{2} \sum_{\text{gas}} m_{\text{gas}} \phi_{\text{gas}}. \quad (12)$$

Here, the summation is over gas cells within the radius of the galaxy, defined as  $2R_{*,1/2}$  (see §2), and  $\phi_{\text{gas}}$  is the gravitational potential at the location of a gas cell. The integration of the right-hand side of Eq. (11) is the cumulative value accounting for both feedback and cooling. Because AGN feedback dominates the feedback energy after  $t_{12}$  (see Eq. 7 and the texts below it), we can obtain  $E_{\text{fdbk}}$  as

$$\begin{aligned} E_{\text{fdbk}} &\approx E_{\text{agn}} = \int \dot{E}_{\text{thermal}} dt \\ &= \int \eta_{\text{thermal}} \dot{M}_{\text{BH}} c^2 dt \approx \eta_{\text{thermal}} M_{\text{BH}} c^2, \end{aligned} \quad (13)$$

where  $\eta_{\text{thermal}} = 0.02$  is the efficiency of the thermal-mode feedback (Weinberger et al. 2018). To exclude the contribution from mergers to  $\dot{M}_{\text{BH}}$  in the estimation of  $E_{\text{agn}}$ , we take the field `BH_CumEgyInjection_QM` from the catalog of TNG to obtain the feedback energy injected by the BH in the thermal mode. The radiative cooling is dominated by star-forming gas cells because of their high density and the sensitive dependence of the cooling rate on gas density. Unfortunately, star-forming gas cells are not resolved by the simulation, which prevents us from computing the cooling rate directly. Weinberger et al. (2018) suggested an alternative way to estimate the cooling loss by subtracting the feedback energy deposited to the star-forming gas cells. This gives a value of  $\eta_{\text{eff}} \approx 10\%-20\%$  for TNG, as shown

in their figure 1. Substituting Eqs. (12) and (13) into Eq. (11), we can obtain the condition for the ending of the fast SMBH accretion as

$$E_{\text{agn}} \gtrsim \eta_{\text{eff}}^{-1} E_{\text{bind}}, \quad (14)$$

where  $\eta_{\text{eff}}^{-1} \approx 5\text{--}10$  for TNG.

Fig. 5 shows the change of  $E_{\text{bind}}$  and  $E_{\text{agn}}$  as a function of time around the transition point  $t_{23}$ . As expected, the total binding energy  $E_{\text{bind}}$  stops increasing at  $t_{23}$ , indicating that part of the gas that flows from the halo to the galaxy is ejected by feedback. The feedback energy  $E_{\text{agn}}$  from AGN starts to rise rapidly at  $\approx 2$  Gyr prior to  $t_{23}$ , consistent with the duration  $\tau_2$  of Phase-2 shown in Fig. 2.  $E_{\text{agn}}$  surpasses  $E_{\text{bind}}$  at  $\approx 0.2$  Gyr prior to  $t_{23}$ , and reaches  $\approx 7 \times E_{\text{bind}}$  at  $t_{23}$ . Thus, the condition given by equation (14) is satisfied, and the fast SMBH accretion is stopped.

The details of the gas ejection by AGN feedback depend on the structure and thermal state of the gas, the coupling of the feedback energy to the gas, and the transfer of energy among gas cells. In TNG, the energy of the thermal-mode feedback is directly deposited to the gas cells surrounding the SMBH and transferred to the outer region via hydrodynamical processes (Weinberger et al. 2017). Thus, the impact of the thermal-mode feedback is inside-out: it significantly reduces the amount of gas surrounding the SMBH, but has smaller effects on outer regions. The three bottom panels of Fig. 6 show the change of the gas mass within different scales. As expected, the gas mass on halo scales, for both the cold and hot components, continues to increase. The mass of the galactic-scale gas stops growing at around  $t_{23}$ . Within  $0.2R_{*,1/2}$ , the cold gas is heated and ejected by the AGN feedback, leading to a reduction of the total gas mass after  $t_{23}$ . The temperature of the gas within the galaxy is raised, but the density drops, as shown in the top right panel of Fig. 6. The significant inside-out change of the gas profile during Phase-2 leads to the cease of SMBH accretion, but only a moderate reduction in star formation, as seen from the top left panel of Fig. 6. The evolutionary path of the galaxy in the  $M_{\text{BH}}-M_*$  plane, as shown by the example in Fig. 2, is then pulled back from nearly vertical to a shallower slope. Note that the results obtained here are consistent with the conclusion of Terrazas et al. (2020) that the thermal-mode AGN feedback primarily regulates the growth of the SMBH, but cannot quench the star formation. Instead, the growth of the galaxy enters into a self-regulated phase, as discussed below.

### 4.3. Phase-3: Self-regulation dominated growth

As the impact volume of AGN feedback expands to the entire galaxy, the gas in the galaxy enters into a regime that is dominated by the AGN feedback. As Bondi accretion depends on the gas properties around the SMBH, the growth of SMBH is self-regulated by

its own feedback. The situation is similar to that reported by Zhuang & Ho (2023, see their figure 4) based on the reconstruction of the star-formation and SMBH-accretion histories for a sample of observed broad-line AGNs. By tracing the evolution of individual systems, we are now able to derive the scaling relations between masses and the conditions to establish them.

#### 4.3.1. The self-regulated growth

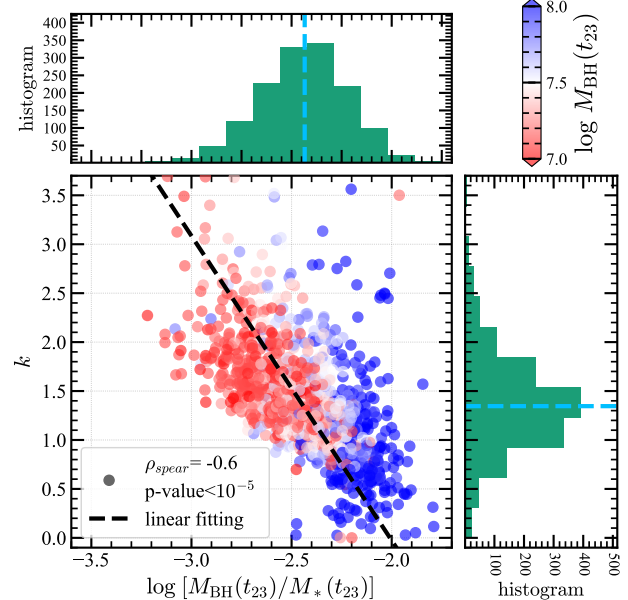


**Figure 7.** The relation between the power-law index,  $k$ , of the  $M_{\text{BH}}-M_*$  history during Phase-3 and the ratio,  $M_{\text{BH}}/M_*$ , at  $t_{23}$ , the beginning of Phase-3. Dots in the **bottom left** panel represent individual galaxies, color-coded by the value of  $M_{\text{BH}}$  at  $t_{23}$ . The Spearman correlation coefficient and the  $p$ -value are indicated in the label. **Black dashed line** shows a linear fit, which gives a slope of about  $-3.0$ . **Top left** and **bottom right** panels show the two marginal distributions, respectively. See §4.3.1 for the details of how this figure implies a self-regulated growth.

The self-regulation nature can be seen from Eq. (14) by considering a perturbation on the gas properties and the consequence of such perturbation on the feedback energy ( $E_{\text{agn}}$ ) and the binding energy ( $E_{\text{bind}}$ ). If gas inflow is temporarily enhanced by, e.g. the fluctuations of halo assembly or the disk instability, Bondi accretion will be accelerated, leading to a trajectory in the  $M_{\text{BH}}-M_*$  plane that resembles the one in Phase-2 and producing an over-massive SMBH. The feedback output then rises, leading to an inequality,  $E_{\text{agn}} > \eta_{\text{eff}}^{-1} E_{\text{bind}}$ . The gas surrounding the SMBH will then be evacuated and the growth of SMBH will be stalled. Inversely, if the gas inflow is suppressed by, e.g. the temporary reduction of halo accretion or the consumption of gas by

star formation, Bondi accretion will be stopped, leading to a shallower trajectory in the  $M_{\text{BH}}-M_*$  plane. The inequality will be inverted as  $E_{\text{agn}} < \eta_{\text{eff}}^{-1} E_{\text{bind}}$ , and so the gas will be accumulated again, and the growth of the SMBH will be accelerated. The discussion here implies that the evolution of the galaxy and its SMBH closely follows a trajectory defined by the equilibrium equation  $E_{\text{agn}} = \eta_{\text{eff}}^{-1} E_{\text{bind}}$ .

To convert this prediction into an explicit relation, we use the virial theorem, and approximate the binding energy as  $E_{\text{bind}} \sim M_{\text{g}} V_{\text{g}}^2$  at the galaxy scale. Combined with the feedback energy given by Eq. (13), we obtain

$$\begin{aligned} \eta_{\text{eff}} \eta_{\text{thermal}} M_{\text{BH}} &\propto M_{\text{g}} V_{\text{g}}^2 \propto f_{\text{gas}} M_{\text{h}}^{5/3} \\ &\propto f_{\text{gas}} f_*^{-5/3} M_*^{5/3}, \end{aligned} \quad (15)$$

where we have defined  $f_{\text{gas}} = M_{\text{g}}/M_{\text{h}}$  and  $f_* = M_*/M_{\text{h}}$ , and used the self-gravitation condition  $V_{\text{g}} \approx V_{\text{h}} \sim M_{\text{h}}^{1/3}$ . Thus, the equilibrium equation can be written as

$$M_{\text{BH}} \sim f M_*^{5/3}, \quad (16)$$

where the scaling factor  $f \equiv \eta_{\text{eff}}^{-1} \eta_{\text{thermal}} f_{\text{gas}} f_*^{-5/3}$ . The values of  $\eta_{\text{eff}}$  and  $\eta_{\text{thermal}}$  depend on the implementation of the feedback model in the simulation, as described in §4.2. One interesting feature of  $f_*$ , as suggested by observations (e.g. Yang et al. 2007, 2012; Behroozi et al. 2019), is the flattening at the critical mass,  $M_{\text{h,c}} \approx 10^{12} \text{ M}_\odot$  (or  $M_{*,\text{c}} \approx 10^{10.5} \text{ M}_\odot$ ), where  $f_*$  appears to be independent of halo mass to the first order. The gas fraction,  $f_{\text{gas}}$ , is also expected to peak at this critical mass, as suggested by (Terrazas et al. 2020; Voit et al. 2024). Thus, at around  $M_{*,\text{c}}$ , all these coefficients are roughly constant, with only moderate redshift dependence introduced by the relation between  $M_{\text{h}}$  and  $V_{\text{g}}$ . Consequently, the equilibrium equation predicts a power-law relation,  $M_{\text{BH}} \propto M_*^{5/3}$ . At lower or higher mass scales,  $f_*$  and  $f_{\text{gas}}$  cannot be viewed as a constant, and the power-law index may deviate from 5/3. Note that the prediction of the scaling relation here is consistent with the semi-analytical model of Mo et al. (2024) and the observationally calibrated toy model of Hong et al. (2023), although they focus on the formation of bulge component and quenched galaxies, respectively.

The example shown by the red dashed curve in Fig. 2 demonstrates the regulation over the equilibrium scaling relation. At  $t_{23}$ , the SMBH mass is slightly overshot relative to the power-law scaling with index  $\gamma = 5/3$ . During Phase-3, the galaxy is pulled back towards the scaling, and finally comes to a region in the  $M_{\text{BH}}-M_*$  plane where other galaxies (shown by grey curves) converge. To statistically quantify the self-regulation nature, in Fig. 7, we show  $k$ , the power-law index of the  $M_{\text{BH}}-M_*$  relation during Phase-3 obtained from the best-fit function (Eq. 2), and  $M_{\text{BH}}(t_{23})/M_*(t_{23})$ , the ratio of SMBH mass and stellar mass at the beginning of Phase-3, for

individual galaxies, as well as the marginal distributions. The distribution of  $M_{\text{BH}}(t_{23})/M_*(t_{23})$  has a median of  $\approx 10^{-2.4}$ , approaching the typical value of galaxies at  $z = 0$ . The distribution of  $k$  has a median of  $\sim 1.35$ , smaller than the value of 5/3 that Eq. (15) would imply if both  $f_{\text{gas}}$  and  $f_*$  are constant. A strong anti-correlation between  $k$  and  $M_{\text{BH}}(t_{23})/M_*(t_{23})$  is seen from the scattered points, and confirmed by the negative (rank-based) Spearman correlation coefficient. The dashed line in Fig. 7 shows a linear regression of  $k$  on  $\log [M_{\text{BH}}(t_{23})/M_*(t_{23})]$ , and has a slope of  $\approx -3.0$ . This slope indicates that, if a SMBH deviates from the equilibrium scaling relation (Eq. 15), it is pulled back once  $M_*$  grows for about 0.3 dex. For a typical main-sequence galaxy at  $z \approx 0$  with  $\text{sSFR} \sim 1 \text{ Gyr}^{-1}$ , this pull-back timescale is  $\sim 2 \text{ Gyr}$ , shorter than the Phase-3 duration of most galaxies (Fig. 2). Hence, most SMBHs are well self-regulated during Phase-3, which erases the footprints of their early growth, including the seeding process. We have performed additional tests using star-forming galaxies at  $z = 0$  whose Phase-3 is well established, and found that the anti-correlation between  $k$  and  $M_{\text{BH}}(t_{23})/M_*(t_{23})$  is still present, not limited by our sample selection (see §2). The self-regulation dominated growth also explains the tight relation between  $M_{\text{BH}}$  and  $M_*$  at  $z = 0$ , as shown by the black solid curve in Fig. 2. Observations also suggest a relation between  $M_{\text{BH}}$  and  $M_*$  (or  $M_{*,\text{bulge}}$ ) in the local Universe (e.g. Kormendy & Ho 2013; Greene et al. 2020; Zhang et al. 2024), which we will discuss in §5.1.

The similar trend of sHAR, sSFR, and sBHAR during Phase-3 shown in the top left panel of Fig. 6 suggests that the rate of evolution of a galaxy in the  $M_{\text{BH}}-M_*$  plane is controlled by the accretion rate of the host halo. The regulation by the AGN feedback bridges the growth pattern of the host halo to the galaxy and SMBH, and leads to the establishment of the scaling relation derived in Eq. (15). The sBHAR decreases with time during Phase-3, as it follows the sHAR that in general decreases with time. Once a certain mass threshold is reached, the mode of AGN feedback implemented in TNG makes a transition, as we will discuss in the following sections.

#### 4.3.2. The trigger of the kinetic-mode feedback

TNG implements a two-mode AGN feedback: a thermal mode at high Eddington ratios and a kinetic mode at low Eddington ratios. The kinetic mode is implemented to effectively transport the feedback energy to the gas at a large scale and to prevent over-cooling of the halo gas (e.g. Weinberger et al. 2017, 2018; Pillepich et al. 2018b). Thus, the transition of AGN feedback from the thermal to the kinetic mode modifies the growth of the galaxy and the SMBH at late times, and is critical in shaping the observational properties, in particular those related to quenching, of low- $z$  galaxies predicted by the simulation. Here, we search for a criterion

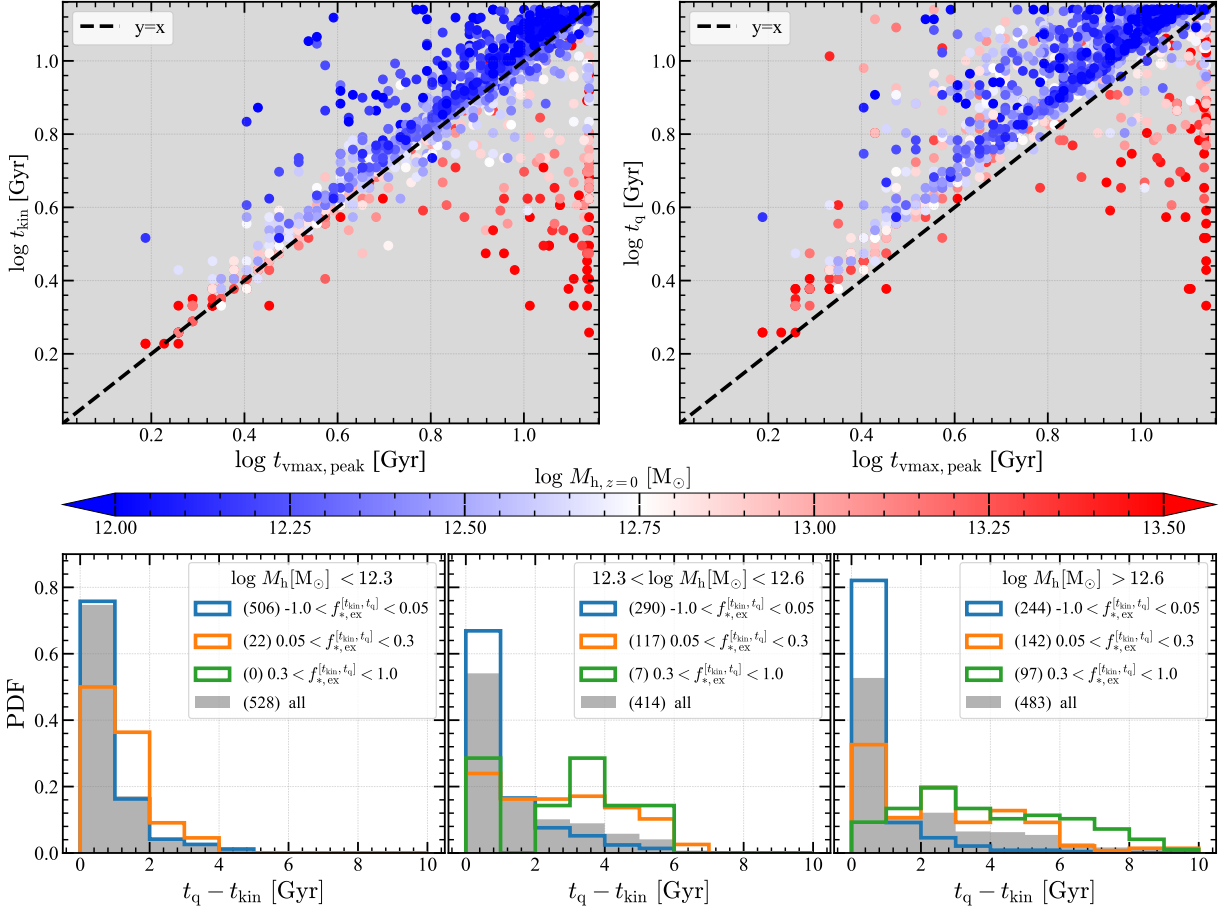


**Figure 8.** Distribution of the properties relevant to the quenching of galaxies. **Top panels** show the distributions of individual galaxies in the  $t_{\text{kin}}-t_{\text{vmax, peak}}$  (left) and  $t_q-t_{\text{vmax, peak}}$  (right) planes, color-coded by their  $M_{\text{h}}$  at  $z=0$ . **Bottom panels** show the histograms of  $t_q - t_{\text{kin}}$ , the time lag of quenching after the trigger of the kinetic-mode feedback. The grey histogram in each panel shows the result for a subsample of galaxies in a given range of  $M_{\text{h}}$  at  $z=0$ . This subsample is further divided into three bins by  $f_{*,\text{ex}}^{[t_{\text{kin}}, t_q]}$ , the ex-situ growth of stellar mass between  $t_{\text{kin}}$  and  $t_q$ , and their histograms are shown in different colors. The number of galaxies in each bin is labeled in the legend. See §4.3.2 and §4.3.3 for the definitions of these times and their implications for galaxy quenching.

for this transition in order to understand how it can relate to the properties of the galaxies and halos at low  $z$ .

In TNG, the kinetic-mode feedback is triggered when the Eddington ratio,  $\chi = M_{\text{BH}}/\dot{M}_{\text{Edd}}$ , falls below a threshold

$$\chi_{\text{thres}} \equiv \min \left[ 0.002 \left( \frac{M_{\text{BH}}}{10^8 M_{\odot}} \right)^2, 0.1 \right], \quad (17)$$

where the  $M_{\text{BH}}$ -dependence is introduced to favor the transition of SMBHs in massive galaxies so that their quenched fraction is consistent with observations, and the upper bound, 0.1, is set to avoid a too-early stop of the SMBH growth in massive galaxies (see §2.1 of Weinberger et al. 2017). By definition, the Eddington limit  $\dot{M}_{\text{Edd}}$  is proportional to  $M_{\text{BH}}$ . If the gas environment is only slowly evolving during Phase-3 (see, e.g. the slow evolution of  $A_s$  in the top right panel of Fig. 6),

$\chi$  is proportional to the sBHAR. According to the self-regulation scenario described in §4.3.1, the evolution of sBHAR follows that of sHAR (see the top left panel of Fig. 6). Thus,  $\chi$  is also roughly proportional to the sHAR.

For low-mass SMBHs (a subsample with  $M_{\text{BH}, z=0} \lesssim 10^8 (2 \times 10^8) M_{\odot}$ , containing 38(578) galaxies, about 2.3 (40.5)% of our total sample, and with a median halo mass of  $M_{\text{h}, z=0} = 10^{11.8} (10^{12.2}) M_{\odot}$ ), the threshold  $\chi_{\text{thres}}$  is close to zero, and thus the transition occurs only if the sHAR approaches zero. A universal feature of halo assembly is the presence of two phases: a fast-accretion phase at high redshift, when the halo potential rapidly deepens, and a slow-accretion phase at low redshift, when the halo potential remains constant or even declines (e.g. Zhao et al. 2003). Thus, for the SMBH in a low-mass halo to trigger the kinetic-mode feedback, its host halo must transit to the slow phase. To ver-

ify that the halo transition indeed leads to the trigger of the kinetic-mode feedback, we follow Zhao et al. (2003) to define the halo transition time as  $t_{\text{vmax, peak}}$ , the time when the maximum of the circular velocity,  $V_{\text{max}}$ , reaches the peak, and we follow Weinberger et al. (2018, see their §3.1) to define whether the AGN feedback is in the thermal or kinetic mode. The last time when the AGN feedback switches from the thermal to kinetic mode is found, and denoted as  $t_{\text{kin}}$ , for each galaxy in our sample. Only two galaxies in our sample are quenched at  $z = 0$  without activating the kinetic-mode feedback, and we remove them from the analyses involving  $t_{\text{kin}}$ . We compare  $t_{\text{kin}}$  with  $t_{\text{vmax, peak}}$  for individual halos, and show the results in the top left panel of Fig. 8, color-coded according to their halo masses at  $z = 0$ . For halos with  $M_{\text{h},z=0} \lesssim 10^{12.5} \text{ M}_{\odot}$ ,  $t_{\text{vmax, peak}}$  correlates well with  $t_{\text{kin}}$ , indicating that the transition of the AGN feedback is indeed driven by the transition of halo accretion.

For massive SMBHs (a subsample with  $M_{\text{BH},z=0} \gtrsim 7 \times 10^8 \text{ M}_{\odot}$ , containing 155 galaxies, about 10.9% of our total sample, and with a median halo mass of  $M_{\text{h},z=0} = 10^{13.4} \text{ M}_{\odot}$ ), the threshold  $\chi_{\text{thres}}$  approaches the upper limit 0.1. The transition of these halos can occur even when they are fast accreting. To derive the condition for their transition, we follow Dekel et al. (2023, see their §5.1) to approximate the specific accretion rate of a fast-accreting halo as

$$\dot{M}_{\text{h}}/M_{\text{h}} \propto M_{\text{h}}^{0.14}(1+z)^{5/2}. \quad (18)$$

This rate depends only weakly on  $M_{\text{h}}$  but strongly on redshift, suggesting that the Eddington ratio of a self-regulated SMBH in a massive halo depends only on redshift. A detailed study by Weinberger et al. (2017, see their figure 6) indeed shows such a strong redshift dependence and weak halo-mass dependence. Given this property of the specific growth rate of halo mass, the condition for the transition of AGN feedback within massive halos becomes

$$\chi \sim (1+z)^{5/2} \sim \chi_{\text{thres}} = 0.1, \quad (19)$$

which depends only on redshift and indicates that SMBHs in massive halos transit roughly at a fixed redshift. The red dots in the top left panel of Fig. 8 for halos with  $M_{\text{h}} \gtrsim 10^{13} \text{ M}_{\odot}$  show that  $t_{\text{vmax, peak}}$  can span a wide range, and many of such halos continue to accrete fast until  $z = 0$ . On the other hand,  $t_{\text{kin}}$  can be much earlier than  $t_{\text{vmax, peak}}$ , with most of the halos located around  $t_{\text{kin}} = 3 \text{ Gyr}$  ( $z \approx 2$ ), which confirms our argument.

The SMBHs in intermediate-mass halos fall between the two extreme cases and the trigger of the kinetic mode is at a time between 3 Gyr and  $t_{\text{vmax, peak}}$ , as shown by the white dots in the top left panel of Fig. 8. We note that this conclusion is a result of the specific choice of  $\chi_{\text{thres}}$  in TNG. If, for example, the threshold  $\chi_{\text{thres}}$  is

set to be a constant of 0.1 for all halos, the transition of the AGN feedback would be earlier for low-mass halos.

### 4.3.3. The quenching of galaxies

The feedback energy in the kinetic mode implemented by TNG affects the gas effectively by both ejection and prevention, and can quickly reduce the amount of star-forming gas in the galaxy and beyond (e.g. Zinger et al. 2020; Shi et al. 2022; Martín-Navarro et al. 2021). Consequently, galaxies are expected to be quenched quickly after the transition of the feedback mode. In the top right panel of Fig. 8, we show  $t_{\text{q}}$ , the time when a galaxy is quenched (see §2 for the definition), and compare it to  $t_{\text{vmax, peak}}$  for individual galaxies. For all galaxies,  $t_{\text{q}}$  is systematically later (larger) than  $t_{\text{kin}}$ , indicating that the kinetic-mode AGN feedback is a necessary condition for quenching central galaxies, and that galaxies may sustain their star formation for some time after the trigger of the kinetic-mode feedback.

To quantify the time needed for the kinetic-mode feedback to quench galaxies, the grey histograms in the three bottom panels of Fig. 8 show the distributions of  $t_{\text{q}} - t_{\text{kin}}$  for halos with different masses at  $z = 0$ . For the least massive halos ( $M_{\text{h},z=0} < 10^{12.3} \text{ M}_{\odot}$ ), the majority of the probability mass is located within 1 Gyr, indicating that their quenching is very rapid. For more massive halos ( $M_{\text{h},z=0} > 10^{12.3} \text{ M}_{\odot}$ ), a long tail emerges in the distribution, indicating that a noticeable fraction of galaxies remain star-forming for more than 4 Gyr after the trigger of the kinetic-mode feedback. The increase of the time lag of quenching,  $t_{\text{q}} - t_{\text{kin}}$ , with increasing halo mass indicates that central galaxies residing in massive halos can acquire star-forming gas via additional channels. As suggested by Mo et al. (2024), a more massive halo remains in the phase of fast accretion down to a lower redshift than a less massive one, and thus is expected to bring in more satellite galaxies that can eventually merge with the central galaxy. As suggested by observations (e.g. Dahlem 1994; Sharma & Theuns 2020) and hydrodynamical simulations (e.g. Capelo & Dotti 2017; Peschken et al. 2020; Karam & Sills 2024), mergers can effectively redistribute angular momentum and induce gas inflow, and also compress the gas to trigger rapid cooling and star formation. The longer time lag of quenching in more massive halos is thus a natural consequence of their higher merger rates. To verify this expectation, we divide the sample of galaxies in each bottom panel of Fig. 8 into subsamples according to the “ex-situ” growth of stellar mass,

$$f_{*,\text{ex}}^{[t_{\text{kin}}, t_{\text{q}}]} \equiv \Delta M_{*,\text{ex}}^{[t_{\text{kin}}, t_{\text{q}}]} / M_{*}(t_{\text{q}}), \quad (20)$$

where  $\Delta M_{*,\text{ex}}^{[t_{\text{kin}}, t_{\text{q}}]}$  is the mass of stars formed ex-situ during the time interval between  $t_{\text{kin}}$  and  $t_{\text{q}}$  and fallen into the galaxy before  $t_{\text{q}}$  via either stripping or merger, and  $M_{*}(t_{\text{q}})$  is the stellar mass of the galaxy at  $t_{\text{q}}$ . We

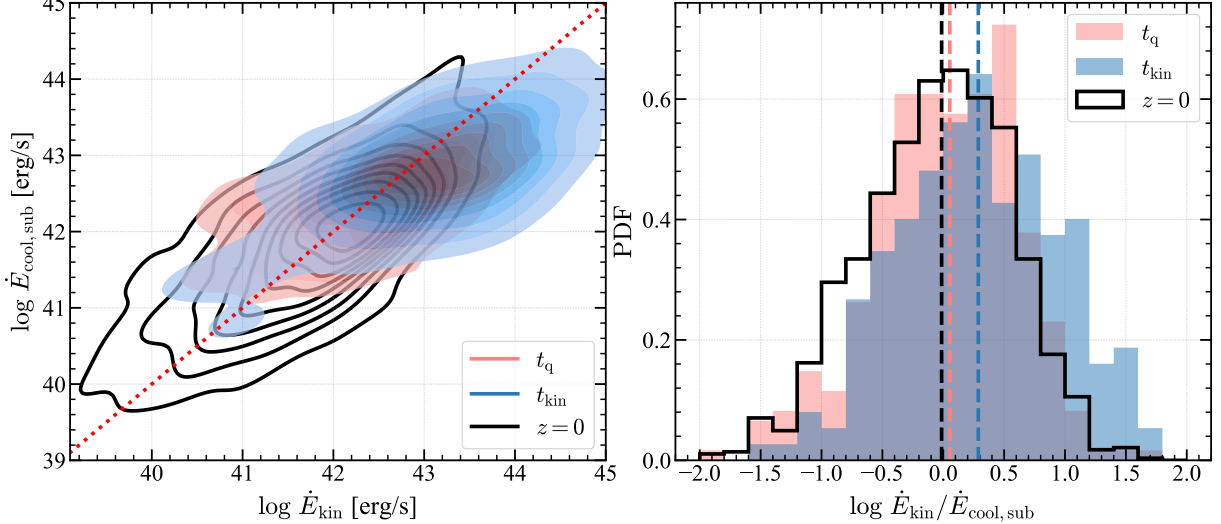


**Figure 9.** The sufficient condition for the quenching of galaxies. **Left panel** shows the distribution of galaxies in the  $\dot{E}_{\text{cool,sub}} - \dot{E}_{\text{kin}}$  plane, where  $\dot{E}_{\text{cool,sub}}$  is the cooling rate of all non-star-forming gas cells in the subhalo, and  $\dot{E}_{\text{kin}}$  is the energy output rate from kinetic-mode AGN. **Contours** with a given color, from inner to outer, encompass 10% – 95% of the galaxies in our sample at a given time point ( $t_{\text{q}}$ ,  $t_{\text{kin}}$  or  $z = 0$ ) during their evolution histories along the main branch. Limited by the data storage, cooling rates are only available in the 20 “full snapshots” of TNG. Thus, the contour for  $t_{\text{kin}}$  (or  $t_{\text{q}}$ ) only includes the galaxies whose  $t_{\text{kin}}$  ( $t_{\text{q}}$ ) is in the “full snapshots”, which reduces the sample size to 199 (304). **Dashed line** indicates where these two rates are equal. **Right panel** shows the histograms of the ratio,  $\dot{E}_{\text{kin}} / \dot{E}_{\text{cool,sub}}$ , at different time points. **Dashed lines** indicate the medians of the distributions. See §4.3.3 for the details.

utilize the published catalog generated by Rodriguez-Gomez et al. (2015) and Rodriguez-Gomez et al. (2016) to identify the ex-situ stars for each galaxy, defined as those bound to the galaxy but formed outside the main branch of the subhalo merger tree rooted in the galaxy. The distribution of the time lag of quenching for each subsample is shown in the bottom panels of Fig. 8 by a colored histogram. For galaxies with  $f_{*,\text{ex}}^{[t_{\text{kin}}, t_{\text{q}}]} < 5\%$ , the time lag is sharply peaked within 1 Gyr, regardless of the halo mass. This demonstrates that the kinetic-mode feedback is indeed effective in quenching the galaxy in the absence of merger-induced gas inflow. However, for galaxies with strong mergers ( $f_{*,\text{ex}}^{[t_{\text{kin}}, t_{\text{q}}]} > 30\%$ ), star formation can sustain a long time, even if the kinetic-mode feedback is triggered. The quenching of a galaxy is thus delayed to a time when the frequency of mergers falls below a certain level, depending on the sSFR threshold used to define the quenching (§2). A similar conclusion was reached by Terrazas et al. (2020), where the cumulative energy of AGN is computed and compared to the binding energy of the gas in a galaxy. Galaxies are found to be quenched only when the feedback energy exceeds about 100 times the binding energy of the gas, indicating that most of the feedback energy is lost due to radiative cooling.

The cease of the merger marks the end of the stochastic creation of star-forming gas, leaving the cooling of hotter gas in a halo being the only channel for the central galaxy to maintain its star formation. In this case, the gas surrounding the SMBH is dominated by that

in the hot phase, as shown in the bottom right panel of Fig. 6. If the energy injection by the kinetic-mode feedback remains strong even when the amount of gas available for the SMBH to accrete is small, as is the case in TNG because of its large feedback efficiency at low accretion rates (Weinberger et al. 2017, see their §2.3), the amount of the gas within the galaxy will continue to decrease due to both ejection and prevention, causing the rates of gas cooling and star formation to slow down. As shown in the top-right panel of Fig. 6, the effective sound speed of the gas during Phase-3 continues to increase, while the density decreases, both leading to a decrease in  $A_s$  and thus to the growth of the SMBH and the strength of its feedback. Such an evolution stops once the feedback of AGN is reduced to a level comparable to the cooling rate of the gas. This final stage, where cooling, star formation, SMBH growth, and AGN feedback are all slow, produces a quenched state that is consistent with observations.

The above argument leads to an equality that characterizes the condition for the kinetic-mode AGN feedback to maintain the quenching of a galaxy without significant mergers, which is that the feedback balances the cooling of gas:

$$\dot{E}_{\text{cool,sub}} = \dot{E}_{\text{kin}}, \quad (21)$$

where  $\dot{E}_{\text{cool,sub}}$  is the total cooling rate of all non-star-forming gas cells within the host subhalo of the galaxy,  $\dot{E}_{\text{kin}} \equiv \eta_{\text{kin}} \dot{M}_{\text{BHC}} c^2$  is the energy output rate of the kinetic-mode AGN, and  $\eta_{\text{kin}} = \min[\rho/(0.05\rho_{\text{SF, thresh}}), 0.2]$  is a coupling efficiency

(Weinberger et al. 2018, see their Eq. 5). The inclusion of the subhalo gas outside the galaxy is necessary for TNG, as its kinetic-mode feedback works through both ejection and prevention over a large scale. The contours in the left panel of Fig. 9 show the distribution of galaxies in the  $\dot{E}_{\text{cool,sub}}-\dot{E}_{\text{kin}}$  plane at different epochs, while the histograms in the right panel show the marginal distributions of  $\dot{E}_{\text{kin}}/\dot{E}_{\text{cool,sub}}$ , both in logarithmic scales. As expected, at the trigger time of the kinetic-mode feedback,  $t = t_{\text{kin}}$ , both  $\dot{E}_{\text{kin}}$  and  $\dot{E}_{\text{cool,sub}}$  are systematically larger than those at later times. In particular,  $\dot{E}_{\text{kin}}$  is larger than  $\dot{E}_{\text{cool,sub}}$ , indicating a non-equilibrium and the continuing reduction of gas. At the quenching point,  $t = t_{\text{q}}$ , the two rates become balanced, both significantly smaller than those at  $t_{\text{kin}}$ , implying a stable state of quenching and the transition of the galaxy into the final phase.

#### 4.4. Phase-4: Merger dominated growth

The final stage of the evolution is a quenched phase. In this phase, the in-situ growth of SMBHs and galaxies ceases, while the ex-situ growth driven by galaxy-galaxy and SMBH-SMBH mergers continues. In the top left panel of Fig. 10, we show the distribution of  $f_{*,\text{ex}}^{[t_{\text{q}}, t_{\text{z}=0}]}$ , the fraction of ex-situ growth of stellar mass between  $t_{\text{q}}$  and  $z = 0$ , defined similarly to Eq. (20) but with a different time interval, for halos with different  $M_{\text{h},z=0}$ . For comparison, in the other three panels, we show the distributions of the fraction of in-situ growth of stellar mass (bottom left), and the ex- and in-situ growth of SMBH mass (right column), respectively. For the ex-situ growth of stellar mass, a clear trend with halo mass is seen, with more massive halos having a larger fraction of ex-situ growth after quenching. This is expected as a consequence of the larger number of satellite galaxies in more massive halos (e.g. Yang et al. 2009, 2012; Wang et al. 2024c) carried in by halo-halo mergers. For halos with  $M_{\text{h},z=0} \geq 10^{12.6} M_{\odot}$ , there are cases where the ex-situ fraction exceeds 80%, indicating that the final properties of the central galaxies in these halos are shaped by their merger histories. These merger-dominated galaxies are expected to form in massive halos with late formation times, as shown by Chen et al. (2023) using an N-body simulation constrained by the density field that matches the observed structures found in SDSS (Wang et al. 2016). A plausible example is the Coma cluster, whose central subhalo appears at  $z \approx 5$ , a relatively late time in comparison with other massive halos, and then grows rapidly via a large number of major mergers. The BCG of Coma is thus likely to reside in the tail of the distribution of  $f_{*,\text{ex}}^{[t_{\text{q}}, t_{\text{z}=0}]}$ . On the other hand, the fraction of in-situ growth of stellar mass since  $t_{\text{q}}$  is nearly independent of halo mass, and nearly always below 20%. Earlier works have suggested that significant in-situ growth of stellar mass can be induced by mergers, via the perturbation of angular momentum and the compression of gas by shocks (e.g. Capelo & Dotti 2017;

Lagos et al. 2018). Our result here suggests that, in TNG, the in-situ growth of stellar mass in galaxies that have already become “dry” (gas-poor) is insignificant.

The distribution of in- and ex-situ fractions of  $M_{\text{BH}}$  growth is similar to those of  $M_{*}$ . Specifically, the ex-situ fraction of  $M_{\text{BH}}$  growth increases with  $M_{\text{h},z=0}$ , and in extreme cases, can exceed 80%. The in-situ fraction of  $M_{\text{BH}}$  growth is always small, nearly zero, due to the strong kinetic-mode feedback that clears the gas surrounding the SMBH. The result here is consistent with Weinberger et al. (2018, see their §4.1 and Fig. 7), where the growth of SMBHs in massive halos experiences a transition, from being dominated by in-situ accretion during the phase of thermal-mode feedback to being dominated by mergers during the phase of kinetic-mode feedback. As mergers tend to bring galaxies into a 1:1 relation in the  $M_{\text{BH}}-M_{*}$  plane, the  $M_{\text{BH}}-M_{*}$  scaling relation is expected to be modified during Phase-4. We will discuss this in §5.1.

As the kinetic-mode AGN feedback in TNG is designed to sustain the quenching of massive galaxies via the self-regulated accretion (Weinberger et al. 2017), the sufficient condition (Eq. 21) of feedback-cooling balance for quenching should remain valid over the entire phase of the quenched evolution. The black contour in Fig. 9 shows a comparison of the cooling rate within the subhalo and the feedback energy rate at  $z = 0$ . Both rates are shifted to lower values relative to those at  $t_{\text{q}}$ , but remain around the balance line. Indeed, observations have suggested that the atmosphere of massive galaxies is in a state of marginally stable to form cold clouds, and the baryon cycling induced by self-regulating AGN feedback is capable of explaining the observed quasi-equilibrium state of massive galaxies (see, e.g. Donahue & Voit 2022, for a review). A similar conclusion was reached by Zinger et al. (2020) using TNG, where gas entropy is used to quantify the effect of AGN feedback. Since high-entropy gas can have high temperature and thus high specific internal energy to be dispersed before forming stars, and have low cooling rate due to the high resistance to compression, the use of entropy as a proxy for the feedback effect is intuitive. Their results show that the entropy of the gas in the circumgalactic medium (CGM) of massive galaxies is significantly lifted by the kinetic-mode feedback out to a distance of several hundred kiloparsecs, so that quenching can be sustained. An interesting side effect of the large-scale kinetic-mode feedback, as proposed by Martín-Navarro et al. (2021), is the reduction of ram pressure stripping of satellite galaxies along the minor axes of the central galaxies where the gas is preferentially cleared by the feedback from the central galaxies. However, as clearly demonstrated by Kang et al. (2007) and Karp et al. (2023), the angular variation of subhalo properties in halos also produces significant anisotropy in the properties of satellite galaxies around central galaxies. A careful subtraction of the effects of subhalo anisotropy

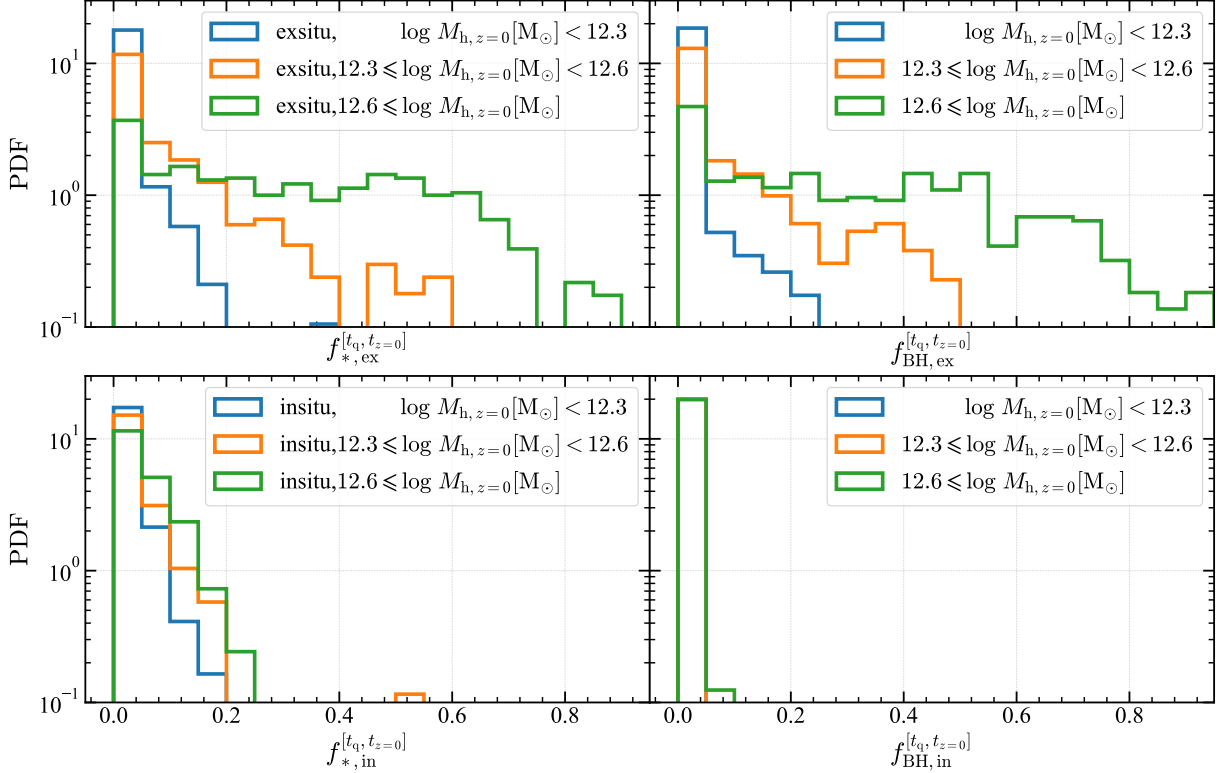


**Figure 10.** Distributions of the ex-situ (**upper row**) and in-situ (**bottom row**) fractions of  $M_*$  (**left column**) and  $M_{\text{BH}}$  growth (**right column**), all evaluated within the time interval between  $t_q$  and  $z = 0$ . In each panel, histograms with different colors show the distributions of galaxies with different  $M_h$  at  $z = 0$ . This figure suggests that the growth of galaxies and SMBHs after quenching (during Phase-4) is dominated by mergers, especially for massive halos. See §4.4 for the details.

is thus necessary to isolate the effect of the AGN feedback on satellite galaxies at large scales.

## 5. RECONSTRUCTING THE PHASES OF SMBH GROWTH FROM OBSERVATIONS

### 5.1. The build-up of scaling relations

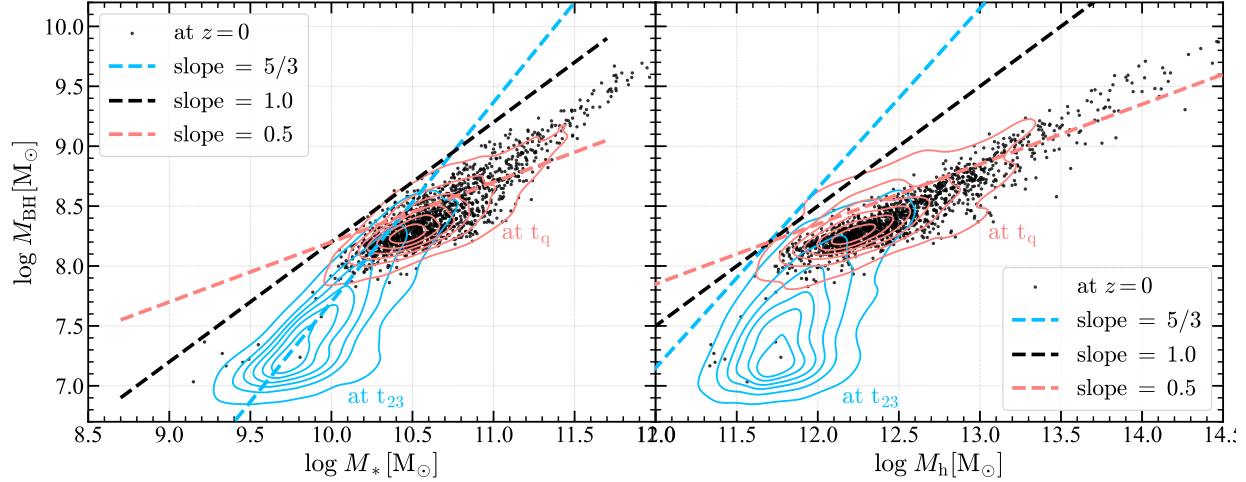
As discussed in §4, the evolution of a SMBH (and its host galaxy/halo) involves a series of critical times that mark the transitions under specific conditions. In the  $M_{\text{BH}}-M_*$  (or  $M_{\text{BH}}-M_h$ ) plane, these conditions form a series of edges that a SMBH has to pass before it can reach subsequent phases. SMBHs with different initial conditions start at different positions in the plane, “flow” in the plane following different paths, and cross the edges at different locations and times. Thus, the  $M_{\text{BH}}-M_*$  (or  $M_{\text{BH}}-M_h$ ) scaling relations at a given epoch for a population of SMBHs in a given phase can be viewed as a time slice of the flow lines in the plane between the two edges that bracket the phase in question. If observations are able to obtain such slices of different redshifts, the locations of the edges can be inferred, thus providing constraints on the physical processes that drive the transitions in the evolution.

Fig. 11 shows the distributions of SMBHs in the  $M_{\text{BH}}-M_*$  and  $M_{\text{BH}}-M_h$  planes at three times:  $t_{23}$ , when the fast accretion of SMBH ends,  $t_q$  ( $\equiv t_{34}$ ), when the galaxy

is quenched, and  $z = 0$ . As discussed in §4.2, the transition at  $t_{23}$  happens when the thermal-mode feedback of AGN is able to unbind the gas of the galaxy. According to Eqs. (14) and (15), this corresponds to a condition of

$$\eta_{\text{eff}} \eta_{\text{thermal}} M_{\text{BH}} \gtrsim f_{\text{gas}} M_{\text{h}}^{5/3} = f_{\text{gas}} f_*^{-5/3} M_*^{5/3}, \quad (22)$$

which predicts a power-law relation between  $M_{\text{BH}}$  and  $M_*$  (or  $M_h$ ), with a power index  $\gamma = 5/3$  at the time when the star formation efficiency peaks, or a different index if  $f_{\text{gas}}$  and  $f_*$  are mass-dependent. As shown by the blue contours in the left panel of Fig. 11, the  $M_{\text{BH}}-M_*$  relation at  $t_{23}$  follows a power-law with a power index of about 5/3. This implies a nearly constant  $f_{\text{gas}} f_*^{-5/3}$  at around  $t_{23}$ , and suggests that the gas and stellar masses are positively correlated. At  $M_* \approx 10^{10} M_\odot$  and  $M_{\text{BH}} \approx 10^7 M_\odot$ , there is a population of SMBHs that deviates from the relation. As noted in §3, this is mainly due to the difficulty in determining  $t_{23}$  accurately. On the other hand, as shown by the blue contours in the right panel, the  $M_{\text{BH}}-M_h$  relation in logarithmic scales appears to be non-linear even for SMBHs with  $M_{\text{BH}}$  well above  $10^7 M_\odot$ . This reflects the non-linear dependence of  $f_{\text{gas}}$  on  $M_h$ . At about  $M_h = M_{h,c} = 10^{12} M_\odot$ ,  $f_{\text{gas}}$  reaches its peak, leading to a  $M_{\text{BH}}-M_h$  relation that follows the power-



**Figure 11.**  $M_{\text{BH}}-M_*$  (left panel) and  $M_{\text{BH}}-M_h$  (right panel) relations at different time points,  $t_{23}$  (blue contours),  $t_q$  (red contours), and  $z = 0$  (black dots), in the histories of the galaxies. In each panel, three dashed lines indicate three relations with different logarithmic slopes. Contours from inner to outer enclose 10% – 95% of the sample. See §5.1 for the details about the build-up of these relations.

law of  $\gamma = 5/3$ . At lower or higher  $M_h$ , the dependence of  $f_{\text{gas}}$  on  $M_h$  changes, which results in bending in the  $M_{\text{BH}}-M_h$  relation.

As concluded in §4.3, the evolution of SMBHs between  $t_{23}$  and  $t_q$  is self-regulated so as to follow  $M_{\text{BH}} \propto M_*^{5/3}$ . Naively one would expect that the  $M_{\text{BH}}-M_*$  relation at  $t_q$  follows the same power law. However, as shown by the red contours in the left panel of Fig. 11, the  $M_{\text{BH}}-M_*$  relation at  $t \sim t_q$  appears to be much shallower, with  $\gamma < 1$ . As discussed in §4.3.2, the trigger of the kinetic-mode feedback is controlled by the  $M_{\text{BH}}$ -dependent threshold of the Eddington ratio,  $\chi_{\text{thres}}$ , for SMBHs with  $M_{\text{BH}} \lesssim 7 \times 10^8 M_\odot$ . It can also be seen from Fig. 8 that the majority of galaxies are quenched soon (within  $\approx 1$  Gyr) after the trigger of the kinetic-mode feedback for halos with  $M_h < 10^{12.3} M_\odot$ . In TNG,  $\chi_{\text{thres}}$  is set so that the kinetic-mode feedback is triggered preferentially for high-mass SMBHs. Thus, the quenching of high-mass galaxies occurs earlier than that expected from a model with a constant (and small)  $\chi_{\text{thres}}$ . The shallow  $M_{\text{BH}}-M_*$  relation at  $M_* \lesssim 10^{11} M_\odot$  is a direct consequence of the choice of the  $\chi_{\text{thres}}-M_{\text{BH}}$  relation. For higher masses ( $M_{\text{BH}} \gtrsim 7 \times 10^8 M_\odot$ ), the threshold  $\chi_{\text{thres}}$  reaches the upper limit, 0.1, and becomes independent of  $M_{\text{BH}}$ . Meanwhile, the conditions necessary for the quenching of galaxies in high-mass halos are delayed by frequent mergers (§4.3.3). Eventually, the preference for quenching in high-mass galaxies is weakened, which allows the SMBHs in them to grow further. The tip present in the red contours at  $M_* \gtrsim 10^{11} M_\odot$  in the left panel of Fig. 11 verifies this. The  $M_{\text{BH}}-M_h$  relation at  $t_q$ , as shown in the right panel, appears as shallow as  $\gamma = 0.5$ . The difference in the index between  $M_{\text{BH}}-M_*$  and  $M_{\text{BH}}-M_h$  relations at  $t_q$  can be understood by an argument similar to that used for

the bending  $M_{\text{BH}}-M_h$  relation at  $t_{23}$ , but here both  $f_{\text{gas}}$  and  $f_*$  decrease with increasing  $M_h$  at  $M_h \gtrsim 10^{12} M_\odot$ .

The evolution of SMBHs (and their host galaxies) in the final phase after  $t_q$  is dominated by the ex-situ growth. As shown in §4.4, the fraction of ex-situ growth for both  $M_{\text{BH}}$  and  $M_*$  depends significantly on the halo mass at  $z = 0$ . This mass dependence implies that the growth of SMBHs and galaxies in low-mass halos is almost frozen after  $t_q$ , while the growth in massive halos is not. The net effect is a “stretch” of the  $M_{\text{BH}}-M_*$  relation towards the high-mass end from an anchor point at the low-mass end, as shown by the black dots in the left panel of Fig. 11. As mergers tend to give a 1:1 relation between the involved masses, the  $M_{\text{BH}}-M_*$  and  $M_{\text{BH}}-M_h$  relations at the most massive ends steepen relative to those at  $t_q$ . The history of the scaling relations is then erased by mergers, leaving behind little trace of the seeding and early growth of the SMBHs.

The TNG subgrid model for AGN feedback is designed to reproduce the observed  $M_{\text{BH}}-M_{*,\text{bulge}}$  relation of Kormendy & Ho (2013), which is a power-law form with an index of  $\gamma \approx 1$ . As shown by Weinberger et al. (2017, see their figure 5), the  $M_{\text{BH}}-M_{*,\text{bulge}}$  relation of the TNG model roughly follows the  $\gamma = 1$  relation, and so does the  $M_{\text{BH}}-M_*$  relation. Since current observational results still have significant uncertainties in estimating the SMBH and bulge masses, it is still unclear whether or not the observed  $M_{\text{BH}}-M_*$  (or  $M_{*,\text{bulge}}$ ) relation can be extended to lower SMBH masses, and what the power index really is. In a more recent work, Greene et al. (2020) suggested a steeper relation,  $M_{\text{BH}} \sim M_*^{1.33}$  for early-type galaxies. Graham & Sahu (2023a, see their table 2) obtained  $M_{\text{BH}} \sim M_*^{1.69}$  (and  $M_{\text{BH}} \sim M_{*,\text{bulge}}^{1.64}$ ) for pure elliptical galaxies. For the  $M_{\text{BH}}-M_h$  relation, Voit et al. (2024) showed that the prediction from TNG is significantly flatter than observations. For the model

to match the observations, they suggested modifications of the criteria for the triggering of the kinetic-mode feedback and/or the feedback efficiency. These more recent observations in the nearby Universe can thus put constraints on the subgrid physics to be implemented in the next generation of simulations, especially for the SMBH growth in the phase of quenched evolution.

Since mergers in the quenched phase erased the imprints of early evolution, in particular for SMBHs in massive halos, a slice of the  $M_{\text{BH}}-M_*$  (or  $M_{\text{BH}}-M_h$ ) flow lines in the nearby Universe may not be adequate to infer the full tracks of galaxies. This can be seen by comparing our TNG-based conclusions to those inferred by [Graham & Sahu \(2023a\)](#), see their figures 8 and 9) from the observed  $M_{\text{BH}}-M_{*,\text{bulge}}$  relations for galaxies with different morphological types. At  $M_{*,\text{bulge}} \gtrsim 10^{11} M_\odot$ , their analysis suggests that mergers between elliptical galaxies (with bulge-to-total ratio  $\approx 1$ ) tend to drive migrations in the  $M_{\text{BH}}-M_{*,\text{bulge}}$  plane towards a 1:1 relation, consistent with our inferences from the TNG. However, our analysis suggests that, for galaxies with  $M_* \lesssim 10^{10.5} M_\odot$ , the ex-situ growth in both  $M_*$  and  $M_{\text{BH}}$  contributes little to the total mass, which is inconsistent with the merger-driven scenario for the formation of elliptical galaxies and the build-up of the  $M_{\text{BH}}-M_{*,\text{bulge}}$  relation in the low-mass end. One possibility is that the dynamical hotness of these galaxies comes from the fast inflow of gas associated with the fast regime of halo assembly (e.g. [Zhao et al. 2003](#)), as suggested by [Mo et al. \(2024\)](#), see also [Yu et al. 2023](#)). The change of the power index of the  $M_{\text{BH}}-M_*$  relation at  $t_q$ , as demonstrated in this paper, is then expected to occur if the kinetic-mode feedback drives the quenching of galaxies.

One way to circumvent the erasure of the long-term evolutionary history by mergers is to find alternative observational indicators in the nearby Universe that can separate in-situ and ex-situ components of the stellar mass. As mergers tend to create dynamically hot stellar orbits, the in-situ and ex-situ growth of stellar mass may be disentangled by decomposing a galaxy into different dynamical components. Indeed, using IllustrisTNG and EAGLE simulations, [Zhu et al. \(2022\)](#) analyzed the consequence of galaxy mergers and found that the mass of the “hot inner stellar halo” is a good indicator of the stellar mass of ex-situ origin. With high-quality IFU observations, such a decomposition can be made by, e.g. the maps of stellar mass, kinematics, metallicity, and age ([Zhu et al. 2020](#)). Scaling relations can then be built between the SMBH mass and the masses of different stellar components.

On the other hand, observations directly targeting SMBHs at high  $z$ , where they are less massive and more active, are crucial to cover the early transitions/edges in the evolutionary history of the SMBH growth and to avoid the ambiguity in the extrapolation of the local scaling relations. Using the deep imaging and spectroscopy capabilities of JWST, [Wang et al. \(2024b\)](#)

found a galaxy with a spectrum compatible with that produced by a Pop-III star cluster. As theoretical studies (e.g. [Stacy et al. 2016](#); [Wise et al. 2019](#); [Chon & Omukai 2020](#); [Latif et al. 2022a,b](#); [Regan & Volonteri 2024](#); [Ventura et al. 2024](#)) have suggested that massive Pop-III stars are promising SMBH seeds of intermediate masses ( $\sim 10^4 M_\odot$ ), direct observations of Pop-III stars (clusters) will be crucial to distinguish among different seeding scenarios (see, e.g. [Spinosa et al. 2023](#)) and to probe the growth of SMBHs in Phase-1.

A recent breakthrough in the observations of SMBHs at high  $z$  with JWST is the discovery of an abundant population of “little red dots” (e.g. [Matthee et al. 2024](#)). Most of these sources have spatial extents of less than 1 kpc, and their gas densities are expected to be sufficiently high to support fast accretion by SMBHs. Indeed, the spectral features, as suggested by [Li et al. \(2024b\)](#), are consistent with low-mass SMBHs that accrete at about the Eddington rate and reside in extended, dusty environments produced by recent star formation and modified by the AGN feedback. These systems are thus likely to be SMBHs in their Phase-2 according to the subgrid model of TNG. Follow-up observations and analyses of these sources are needed to obtain the SMBH mass function, accretion rates, and the properties of their host galaxies, so as to determine when and how Phase-2 starts and ends.

## 5.2. Inferring the paths of SMBH growth from observations

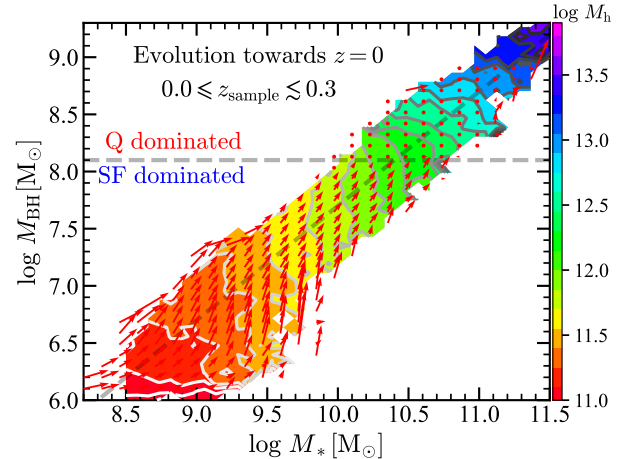


**Figure 12.** Distribution and movement of galaxies in the  $M_{\text{BH}}-M_*$  plane. **2-D histogram** is shown for all central galaxies in TNG with  $M_* \gtrsim 10^{8.5} M_\odot$  at  $z = 0$ . Colors are encoded and contours are drawn to show their host halo masses. **Red arrows** are path segments of these galaxies from  $z = 0.3$  to  $z = 0$ . Tilted **dashed line** shows the  $M_{\text{BH}}-M_{*,\text{bulge}}$  relation found in observation by [Kormendy & Ho \(2013\)](#). See §5.2 for a detailed discussion.

The discussion in §5.1 only requires the measurements of masses of SMBHs, galaxies, and halos at different redshifts. The scaling relations built this way only focus on the time slices of the flow lines for a population of SMBHs, but miss the paths of individual SMBHs across these slices. One way to complete the missed information is to additionally incorporate the first derivatives of the masses: HAR, SFR and BHAR. Among them, both the SFR and BHAR can be directly measured, e.g. from the luminosities of the AGN and galaxy in some bands. In contrast, HAR can only be indirectly inferred, e.g. from the galaxy size (Liang et al. 2024), if a well-calibrated empirical relation is available, or from constrained simulations, if the observed tracers of the underlying field are sufficiently fair and dense (e.g. Wang et al. 2016; Tully et al. 2019; Boruah et al. 2022; Dolag et al. 2023; Sawala et al. 2024). The inclusion of the derivatives allows a first-order extrapolation of the locations of SMBHs in the space of masses, and thus provides evolutionary path segments that carry dynamical information about SMBH growth.

Fig. 12 shows the distribution of SMBHs in the  $M_{\text{BH}}-M_*$  plane at  $z = 0$ , with colors and contours encoded according to their host halo masses. For each population of SMBHs with a given  $M_{\text{BH}}$  and  $M_*$ , an arrow is drawn to indicate the movement of its location in this plane since  $z = 0.3$ . To cover larger ranges of  $M_{\text{BH}}$  and  $M_*$  for this narrow redshift interval, we enlarge the sample size by including all branches with  $M_{*,z=0} \geq 10^{8.5} M_\odot$ . Clear trends can be seen in different regions, each containing SMBHs in a given phase discussed in §4. The lower left corner of the plane is populated with SMBHs in Phase-1, where  $M_{\text{BH}}$  is close to the seed mass of  $\sim 10^6 M_\odot$ . The arrows in the region of  $M_* \sim 10^{9.5} M_\odot$  and  $M_{\text{BH}} \lesssim 10^7 M_\odot$  align with the vertical axis, which marks the transition from the star-formation dominated growth to the SMBH-accretion dominated growth (Phase-2). Once SMBHs approach the local scaling relation of  $M_{\text{BH}}-M_*$  from either the upper or lower side, the flow moves along this relation by the self-regulation dominated growth (Phase-3). The prevalence of massive central SMBHs of  $M_{\text{BH}} \sim 10^{8.2} M_\odot$  (Terrazas et al. 2020, see their figure 5) drives the quenching of galaxies and freezes the evolution of the SMBHs in the  $M_{\text{BH}}-M_*$  plane during Phase-4. For the most massive SMBHs, mergers tend to drive a “dry” evolution towards higher masses, although the sample size is not enough at the high-mass end to produce stable flow lines.

Drawing the flow lines in the  $M_{\text{BH}}-M_*$  plane from observations is more challenging, as it requires the measurements of four quantities  $M_{\text{BH}}$ ,  $M_*$ , BHAR and SFR. For a galaxy with inactive SMBH, BHAR is too low to be detected, while for a galaxy with active SMBH, a decomposition of its image and spectrum is needed to separate the contributions from the AGN and stars. The available data thus only provide an incomplete view of

the SMBH populations, together with measurement uncertainties that probably mix flow lines. Thus, caution should be taken when interpreting the results in order to avoid biased conclusions. A recent work by Zhuang & Ho (2023, see their figure 4) indeed achieved this goal by stacking a large sample of AGNs at  $z \leq 0.35$ , with physical properties derived by a simultaneous decomposition of image and spectrum. The set of flow lines they obtained converges to the local scaling relation, thus supporting the results produced by the subgrid model of TNG for the SMBH growth. A noticeable difference between their results and those of TNG is the presence of over-massive black holes lying above the local scaling relation. This difference is either due to uncertainties in their measurements, or due to the strong feedback in TNG that forbids the growth of SMBHs beyond the local scaling relation. Future observations and more precise measurements are needed to pin down the exact reason.

An observationally more accessible way to infer the evolutionary paths is to only use measurements of the mass of different components. One possibility is to use the size of the scatter in the  $M_{\text{BH}}-M_*$  plane to distinguish different phases. This has been suggested by McAlpine et al. (2018), who found that the EAGLE simulation produces a redshift-dependent critical halo mass for the SMBHs to transit from Phase-1 to Phase-2. As Phase-2 has rapid  $M_{\text{BH}}$  growth while Phase-1 and Phase-3 do not, the scatter in  $M_{\text{BH}}$  is expected to be large during Phase-2 relative to its two sides where the slopes of the  $M_{\text{BH}}-M_*$  and  $M_{\text{BH}}-M_h$  relations are shallower. Another possibility is to use multivariate statistical methods, such as the regression of  $M_{\text{BH}}$  on the joint of  $M_*$  and  $M_h$ . This can be seen from the contours in Fig. 12: for  $M_h < 10^{12.3} M_\odot$  (or  $M_* < 10^{10.5} M_\odot$ ), corresponding to  $M_{\text{BH}} < 10^8 M_\odot$ , the contours are almost vertical, indicating that  $M_{\text{BH}}$  does not depend on  $M_h$  once  $M_*$  is fixed. At higher masses, the contours become horizontal, suggesting that the growth of the SMBH is related more to the halo than to the galaxy. Such a change is implied by the transition from Phase-3 (§4.3), where the growth of SMBH is regulated by the thermal-mode feedback that balances the gravity of gas within the galaxy, to Phase-4 (§4.4), where the growth of SMBH is reduced by the kinetic-mode feedback that balances the cooling of the whole central subhalo. Thus, the scale on which the feedback energy is coupled to the surrounding gas is imprinted in the correlation between mass variables. Indeed, Zhang et al. (2024) found an observational trend similar to the contours shown in Fig. 12, using  $M_h$  measured from galaxy-galaxy weak lensing and  $M_{\text{BH}}$  converted from stellar velocity dispersion. The transition mass scales they obtained,  $M_h \sim 10^{12.0} M_\odot$  and  $M_{\text{BH}} \sim 10^{7.4} M_\odot$ , are consistent with our findings from TNG.

## 6. SUMMARY AND DISCUSSION

### 6.1. Main results

In this paper, we used the IllustrisTNG simulation to quantify the co-evolution of SMBHs, their host galaxies, and halos. We focus on galaxies that are quenched at  $z = 0$  (§2) and use the main branches of the merger trees rooted in these galaxies to trace their evolution. We summarize our results and conclusions in the following.

- (i) Although the growth histories of individual galaxies in the  $M_{\text{BH}}-M_*$  plane are diverse, they show regularities represented by four distinct phases. We fit the  $M_{\text{BH}}-M_*$  history of each galaxy in our sample with a function that allows us to separate the four phases and locate the transition points between them. We found that the first two phases are short, about 1-2 Gyr on average, while the last two phases are significantly longer. Each phase is found to be associated with a process that dominates the growth of the SMBH and its host galaxy, and physical conditions can be identified for the transition from one phase to the next (§3).
- (ii) Phase-1 is dominated by star formation and its feedback. The starting point of the SMBH growth depends on the seeding strategy, and cannot be fully constrained by observations currently available. Gas-rich environments resulted from the fast accretion of halos and effective cooling drive rapid star formation, but the SMBH growth is slow due to the low mass of the seed. The sSFR in this phase is higher than the sBHAR, and stellar feedback dominates the total feedback energy. The maximal duration of this phase is determined by the seed mass of SMBH and the gas environment (density and effective sound speed). A galaxy transits to Phase-2 when its sBHAR exceeds the sSFR (§4.1).
- (iii) Phase-2 is dominated by the accretion and thermal-mode feedback of the SMBH. The growth of the SMBH in this phase follows the exponential form expected from the Bondi accretion until the associated AGN feedback becomes sufficiently effective to unbind the gas of the galaxy. The effect of AGN feedback is inside-out, strong on the surroundings of the SMBH and weaker on the whole galaxy and the halo. Galaxies make transitions to Phase-3 when the difference between the cumulative energy gain from feedback and the energy loss due to gas cooling exceeds the binding energy of the gas in the galaxy (§4.2).
- (iv) Phase-3 is dominated by the self-regulation of SMBH growth. The galaxy in this phase is kept in a quasi-equilibrium state where the effective energy gain roughly balances the binding energy of the gas in the galaxy. The regulation corresponds to power-law relations among the masses:  $\eta_{\text{eff}}\eta_{\text{thermal}}M_{\text{BH}} \sim M_{\text{g}}V_{\text{g}}^2 \sim f_{\text{gas}}M_{\text{h}}^{5/3} \sim f_{\text{gas}}f_*^{-5/3}M_*^{5/3}$ . The exact values of the power-law indices depend on the gas fraction, the stellar mass fraction, and the feedback efficiency (§4.3.1).
- (v) The trigger of the kinetic-mode AGN feedback depends on halo mass. It is closely related to the transition of halo assembly from the fast to slow regimes for halos with  $M_{\text{h},z=0} \lesssim 10^{12.5} \text{ M}_\odot$ , and is much earlier than

the transition of halo assembly for more massive halos (§4.3.2). The kinetic-mode AGN feedback is a necessary condition for the quenching of a central galaxy, but quenching can be delayed by mergers. A sufficient condition for the quenching of a galaxy is that the cooling rate of the hot gas in the subhalo is comparable to the energy output rate of the AGN (§4.3.3).

- (vi) Phase-4 is dominated by the ex-situ growth driven by galaxy mergers, with in-situ growth playing a much smaller role.  $M_*$  and  $M_{\text{BH}}$  of ex-situ origin assembled in this phase account for more than 80% of their final values for some galaxies. The balance between the energy output rate of the AGN and the cooling rate within the subhalo is sustained during Phase-4 (§4.4).
- (vii) The power index ( $\gamma$ ) of the  $M_{\text{BH}}-M_*$  relation varies as the dominating processes for the growth of SMBHs and galaxies change between different phases. The value of  $\gamma$  is about 1.5 at  $t_{23}$  due to the condition for the thermal-mode feedback to overcome the potential energy of the gas; it becomes smaller than 1 at  $t_{\text{q}}$  due to the specific choice of TNG for triggering the kinetic-mode feedback; and it is driven back to  $\approx 1$  at  $z = 0$  for high-mass galaxies by mergers. We highlight potential observational tests for the predictions of the simulation. These include the use of scaling relations that bracket the phases and transitions, and the use of the mass growth rates to reconstruct the evolution paths of SMBHs and galaxies (§5).

## 6.2. Implications

We note that our results and conclusions are based on the numerical and subgrid models of IllustrisTNG. How the predicted observables respond to the change of model assumptions is of great interest and is one of the main targets in using hydrodynamical simulations to understand galaxy formation. Such a question has been explored by [Habouzit et al. \(2021\)](#) using a set of different simulations: Illustris, IllustrisTNG, Horizon-AGN, EAGLE and SIMBA. All these simulations produce a  $M_{\text{BH}}-M_*$  relation similar to that observed for high-mass ( $M_* \gtrsim 10^{10.5} \text{ M}_\odot$ ) galaxies at  $z \sim 0$  (e.g. [Kormendy & Ho 2013](#)). Such an agreement is not significant, however, as the observational relation was used to calibrate the model parameters in these simulations. More interesting and significant is that the paths of individual galaxies in the  $M_{\text{BH}}-M_*$  plane before they reach the local scaling relation are different both among different simulations and at different redshifts within a given simulation.

In EAGLE, the  $M_{\text{BH}}-M_*$  relation at both  $z = 3$  and  $z = 0$  is found to be non-linear (in logarithmic scale) and to drop at  $M_* \lesssim 10^{10.5} \text{ M}_\odot$ , reflecting the strong supernova feedback in suppressing the growth of SMBHs (corresponding to our Phase-1) in low-mass galaxies at both redshifts. As discussed in §4.1 and based on the results of [McAlpine et al. \(2017\)](#), the transition from Phase-1 to Phase-2 in EAGLE occurs when the virial temperature of the halo reaches a time-independent crit-

ical value. The corresponding critical halo mass changes moderately from  $M_h \approx 10^{11.2} M_\odot$  at  $z = 6$  to  $10^{12.4} M_\odot$  at  $z = 0$ . At a given redshift, the observed  $M_{\text{BH}}-M_*$  relation at the low-mass end is thus dominated by the insufficient growth of SMBHs in Phase-1, which causes the relation to bend downwards with respect to the local scaling relation.

The situation in TNG is different in that the non-linearity of the  $M_{\text{BH}}-M_*$  relation at the low-mass end appears at  $z = 3$  but disappears at  $z = 0$ . [Habouzit et al. \(2021\)](#) attributed this to the “inefficient” SN feedback at low  $z$  in TNG. We can follow the argument used in deriving  $\tau_1$  in §4.1 to obtain some quantitative understanding, by explicitly incorporating the definition of the transition into the Bondi accretion. Equaling the sBHAR given by the Bondi formula (Eq. 3) to the sSFR, we obtain the SMBH mass at the transition  $t_{12}$  as  $M_{\text{BH}}(t_{12}) = \text{sSFR}(t_{12})/A_s(t_{12})$ . Because  $A_s$  can be approximated as a constant during Phase-1 (see Fig. 3) and the sSFR of star-forming galaxies decreases by  $\gtrsim 1$  dex from  $z = 3$  to  $z = 0$  in TNG (e.g. [Chen et al. 2021](#), see their figure 8),  $M_{\text{BH}}(t_{12})$  is expected to decrease by  $\gtrsim 1$  dex in this redshift range. As seen from Fig. 2, this decrease is sufficient to push  $M_{\text{BH}}(t_{12})$  downwards to a position below the seed mass of SMBHs. Thus, a newly seeded SMBH at low  $z$  skips the entire Phase-1, which makes the  $M_{\text{BH}}-M_*$  relation linear towards the low-mass end. Indeed, for galaxies at  $z \leq 0.3$  shown in Fig. 12, the flow lines at  $M_{\text{BH}} \approx 10^6 M_\odot$  go upwards without a significant horizontal movement, as expected from our argument. Our result also implies that, if a lower seed mass is adopted while keeping other recipes unchanged in TNG, or if the seeding is delayed until a higher halo/stellar mass is reached, the non-linear  $M_{\text{BH}}-M_*$  relation would appear at lower  $z$ . The latter condition is fulfilled in SIMBA, and a non-linear  $M_{\text{BH}}-M_*$  relation towards the low-mass end is indeed found at  $z = 0$  in this simulation ([Habouzit et al. 2021](#), see their figure 11).

In more extreme cases where SN feedback is weak even at high  $z$  or totally absent in the simulation, a newly seeded SMBH would immediately start its rapid growth and Phase-1 is expected to disappear completely. The weak SN feedback adopted by Horizon-AGN is such a case, and indeed the predicted  $M_{\text{BH}}-M_*$  relation at  $z = 3$  is roughly linear ([Habouzit et al. 2021](#), see their figure 11). Numerical experiments of disabling SN feedback by [Bower et al. \(2017\)](#), see their figure 7) also produce such a linear relation.

The duration of Phase-2,  $\tau_2$ , as shown in Fig. 6 and estimated by Eq. (4), is about 1 Gyr. However, this timescale depends on the gas environment around a SMBH, and thus depends on the density threshold of star-forming gas assumed by the simulation, the sub-grid models evolving the cold gas, and the smoothing kernel defining the SMBH neighborhood. The threshold density is  $n_{\text{gas}} \approx 0.1 \text{ cm}^{-3}$  in both EAGLE and TNG,

far below the density that a real galaxy can reach, as inferred both analytically and observationally (see, e.g. §2 of [Chen et al. 2024b](#) and §6 of [Dekel et al. 2023](#)). Lifting this threshold is computationally expensive and thus not feasible for simulations on cosmological scales. Using a set of idealized simulations for individual gas clouds embedded with randomly seeded low-mass BHs, [Shi et al. \(2023\)](#) found that the small-scale structure of a gas cloud can be complex. The runaway collision of a BH with a gas sub-cloud produces a boost of  $M_{\text{BH}}$ , much resembling the rapid growth of Phase-2. The collision can repeat multiple times, leading to a ladder-like growth history of  $M_{\text{BH}}$  (see their figures 1 and 2). Each collision starts and ends within a duration  $\ll 1$  Myr, more than three orders of magnitude shorter than our  $\tau_2$ , and even shorter than the lifetime of massive stars so that SNs are not able to be triggered. On the other hand, [Hopkins et al. \(2024\)](#) conducted a “hyper-refinement” zoom-in simulation for a galaxy within the cosmological context. Asymmetric gas structures around the SMBH are found and sustained super-Eddington accretion flow coexists with outflow. Star-formation within the influence radius of the SMBH is suppressed due to the pressure from turbulence and magnetic field, making star formation and stellar feedback ineffective. The high density and complex sub-structure of gas, the fast and repeated boost of  $M_{\text{BH}}$  by super- or hyper-Eddington accretion within a timescale less than Myr, and the inefficient stellar feedback, all suggest rich physics of Phase-2 that needs to be explored further.

The ending of Phase-2 at  $t_{23}$  by the AGN feedback to unbind the gas (Eq. 22) depends on the (radiative and coupling) efficiency of the feedback energy ( $\eta_{\text{thermal}}$ ) and subsequent cooling of the heated gas ( $\eta_{\text{eff}}$ ). A simulation with different  $\eta_{\text{thermal}}$  and/or  $\eta_{\text{eff}}$  can thus produce a  $M_{\text{BH}}-M_*$  relation at  $t_{23}$  (Fig. 11) with different normalizations. Since the self-regulation of SMBHs during Phase-3 is also determined by these two factors, the normalization of the  $M_{\text{BH}}-M_*$  relation during Phase-3 and at  $t_q$  will also be changed. The difference in the normalization of the scaling relation shown in figure 4 of [Habouzit et al. \(2021\)](#) for different simulations can thus be understood along this line. On the other hand, the power index of the scaling relation at a specific event such as  $t_{23}$  or  $t_q$ , is distorted by the conditions for the event to be triggered. We showed in §5.1 that the kinetic-mode AGN feedback modeled in TNG is preferentially triggered in high-mass halos, which produces a shallow power index of the scaling relation at  $t_q$ . Such a transition in SIMBA does not have a clear mass preference, and thus produces a more widely spread range of  $M_*$  and a non-constant power index.

The final phase, Phase-4, is dominated by the ex-situ, gas-poor growth at the high-mass end. As the frequency of mergers is determined by the hierarchical structure formation in the  $\Lambda$ CDM cosmology, it is not sensitive to baryonic physics and is thus expected to be similar

across simulations. Indeed, all the simulations shown in figure 4 of [Habouzit et al. \(2021\)](#) produce a tip at the high-mass end of the  $M_{\text{BH}}-M_*$  relation, with a power index of  $\approx 1$ . The normalization of this tip, however, inherits the influences of baryonic physics at  $t_q$ , and thus varies with simulations, as seen from the lower normalization of EAGLE. The scaling relation in Phase-4 for low-mass galaxies that have not experienced significant mergers is frozen after  $t_q$ , and thus also depends on the baryonic physics.

In summary, our method based on separating the evolution of galaxies into different phases and identifying transitions between them provides a way to compare different simulations in a unified way. The identification of the driving processes in each phase provides a powerful avenue to connect observations to physical processes, and to improve the relevant subgrid models. We plan to come back to related investigations in the future.

## 7. DATA AVAILABILITY

Data directly related to this publication and its figures are available on request from the corresponding author.

The IllustrisTNG simulations themselves, are publicly available and accessible at [www.tng-project.org/data](http://www.tng-project.org/data).

We thank the referee for a useful report that significantly improved the paper. This work is supported by the National Natural Science Foundation of China (NSFC, Nos. 12192224, and 11890693), CAS Project for Young Scientists in Basic Research (No. YSBR-062), the Fundamental Research Funds for the Central Universities, and the China Postdoctoral Science Foundation (No. 2022TQ0329). We acknowledge the science research grants from the China Manned Space Project with No. CMS-CSST-2021-A03. The authors gratefully acknowledge the support of Cyrus Chun Ying Tang Foundations. HL thanks Kai Wang, Hui Hong, Xiong Luo, Yuan Wang, Enci Wang, Wentao Luo and Yu Rong for their valuable insights and discussions. The work is also supported by the Supercomputer Center of University of Science and Technology of China. The authors would like to express their gratitude to Max Planck Computing and Data Facility (MPCDF) for providing the necessary computational and data storage resources that have significantly contributed to the research results presented in this paper.

## APPENDIX

### A. FITTING ERROR

The definition of the phases and transitions for each galaxy is based on the fitting of the  $M_{\text{BH}}-M_*$  relation in the evolutionary history (§3). Here we examine the quality of the fitting by two measurements of errors, the root-mean-square error (RMSE) and the maximum absolute error (MAE), defined as

$$\text{RMSE}(y_{\text{sim}}, y_{\text{fit}}) = \sqrt{\frac{1}{n} \sum_s (y_{\text{sim},s} - y_{\text{fit},s})^2}, \quad (\text{A1})$$

$$\text{MAE}(y_{\text{sim}}, y_{\text{fit}}) = \max_s \{|y_{\text{sim},s} - y_{\text{fit},s}|\}, \quad (\text{A2})$$

respectively, where  $y_{\text{sim},s}$  and  $y_{\text{fit},s}$  are the simulated and best-fit values of  $\log M_{\text{BH}}$  at snapshot  $s$ . The distributions of these two errors for our example of galaxies (see §2) are shown in Fig. A1. The distribution of RMSE (MAE) peaks at 0.05 (0.1), with most of the probability mass below 0.1 (0.3). Given the large dynamical ranges of  $M_{\text{BH}}$  and  $M_*$ , the small errors suggest that our fitting safely captures the main trend of the evolutionary histories of individual galaxies.

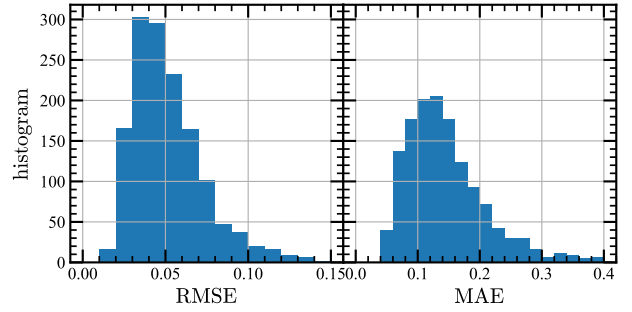


**Figure A1.** The distributions of root-mean-square error (left panel) and maximum absolute error (right panel) of our fitting.

## REFERENCES

Acevedo, J. F., An, H., Boukhtouchen, Y., et al. 2023, Dark Matter-Induced Baryonic Feedback in Galaxies, arXiv, doi: [10.48550/arXiv.2309.08661](https://doi.org/10.48550/arXiv.2309.08661)

Adamo, A., Bradley, L. D., Vanzella, E., et al. 2024, The Discovery of Bound Star Clusters 460 Myr after the Big Bang, doi: [10.48550/arXiv.2401.03224](https://doi.org/10.48550/arXiv.2401.03224)

Agertz, O., & Kravtsov, A. V. 2016, ApJ, 824, 79, doi: [10.3847/0004-637X/824/2/79](https://doi.org/10.3847/0004-637X/824/2/79)

Anglés-Alcázar, D., Faucher-Giguère, C.-A., Quataert, E., et al. 2017, Monthly Notices of the Royal Astronomical Society: Letters, 472, L109, doi: [10.1093/mnrasl/slx161](https://doi.org/10.1093/mnrasl/slx161)

Ayromlou, M., Kauffmann, G., Anand, A., & White, S. D. M. 2023, MNRAS, 519, 1913, doi: [10.1093/mnras/stac3637](https://doi.org/10.1093/mnras/stac3637)

Bandara, K., Crampton, D., & Simard, L. 2009, The Astrophysical Journal, 704, 1135, doi: [10.1088/0004-637X/704/2/1135](https://doi.org/10.1088/0004-637X/704/2/1135)

Baugh, C. M., Gonzalez-Perez, V., Lagos, C. D. P., et al. 2019, MNRAS, 483, 4922, doi: [10.1093/mnras/sty3427](https://doi.org/10.1093/mnras/sty3427)

Behroozi, P., Wechsler, R. H., Hearn, A. P., & Conroy, C. 2019, MNRAS, 488, 3143, doi: [10.1093/mnras/stz1182](https://doi.org/10.1093/mnras/stz1182)

Behroozi, P. S., Wechsler, R. H., & Conroy, C. 2013, ApJ, 770, 57, doi: [10.1088/0004-637X/770/1/57](https://doi.org/10.1088/0004-637X/770/1/57)

Bik, A., Álvarez-Márquez, J., Colina, L., et al. 2024, Astrophysical Journal, 686, A3, doi: [10.1051/0004-6361/202348845](https://doi.org/10.1051/0004-6361/202348845)

Blank, M., Macciò, A. V., Dutton, A. A., & Obreja, A. 2019, MNRAS, 487, 5476, doi: [10.1093/mnras/stz1688](https://doi.org/10.1093/mnras/stz1688)

Bluck, A. F. L., Conselice, C. J., Ormerod, K., et al. 2024, ApJ, 961, 163, doi: [10.3847/1538-4357/ad0a98](https://doi.org/10.3847/1538-4357/ad0a98)

Blumenthal, G. R., Faber, S. M., Primack, J. R., & Rees, M. J. 1984, Nature, 311, 517, doi: [10.1038/311517a0](https://doi.org/10.1038/311517a0)

Bogdán, Á., & Goulding, A. D. 2015, The Astrophysical Journal, 800, 124, doi: [10.1088/0004-637X/800/2/124](https://doi.org/10.1088/0004-637X/800/2/124)

Boruah, S. S., Lavaux, G., & Hudson, M. J. 2022, MNRAS, 517, 4529, doi: [10.1093/mnras/stac2985](https://doi.org/10.1093/mnras/stac2985)

Bower, R. G., Schaye, J., Frenk, C. S., et al. 2017, MNRAS, 465, 32, doi: [10.1093/mnras/stw2735](https://doi.org/10.1093/mnras/stw2735)

Byrne, L., Faucher-Giguère, C.-A., Stern, J., et al. 2023, MNRAS, 520, 722, doi: [10.1093/mnras/stad171](https://doi.org/10.1093/mnras/stad171)

Capelo, P. R., & Dotti, M. 2017, MNRAS, 465, 2643, doi: [10.1093/mnras/stw2872](https://doi.org/10.1093/mnras/stw2872)

Chen, Y., Mo, H., & Wang, H. 2024a, MNRAS, 532, 4340, doi: [10.1093/mnras/stae1757](https://doi.org/10.1093/mnras/stae1757)

—. 2024b, A Two-Phase Model of Galaxy Formation: III. The Formation of Globular Clusters, arXiv. <https://arxiv.org/abs/2405.18735>

Chen, Y., Mo, H. J., Li, C., et al. 2019, ApJ, 872, 180, doi: [10.3847/1538-4357/ab0208](https://doi.org/10.3847/1538-4357/ab0208)

—. 2021, MNRAS, 507, 2510, doi: [10.1093/mnras/stab2377](https://doi.org/10.1093/mnras/stab2377)

Chen, Y., Mo, H. J., & Wang, K. 2023, MNRAS, 526, 2542, doi: [10.1093/mnras/stad2866](https://doi.org/10.1093/mnras/stad2866)

Chon, S., & Omukai, K. 2020, MNRAS, 494, 2851, doi: [10.1093/mnras/staa863](https://doi.org/10.1093/mnras/staa863)

Croton, D. J., Stevens, A. R. H., Tonini, C., et al. 2016, ApJS, 222, 22, doi: [10.3847/0067-0049/222/2/22](https://doi.org/10.3847/0067-0049/222/2/22)

Cui, W., Davé, R., Peacock, J. A., Anglés-Alcázar, D., & Yang, X. 2021, Nature Astronomy, 5, 1069, doi: [10.1038/s41550-021-01404-1](https://doi.org/10.1038/s41550-021-01404-1)

Dahlem, M. 1994, AIP Conference Proceedings, 313, 333, doi: [10.1063/1.46740](https://doi.org/10.1063/1.46740)

Davé, R., Anglés-Alcázar, D., Narayanan, D., et al. 2019, MNRAS, 486, 2827, doi: [10.1093/mnras/stz937](https://doi.org/10.1093/mnras/stz937)

Dekel, A., Sarkar, K. C., Birnboim, Y., Mandelker, N., & Li, Z. 2023, MNRAS, 523, 3201, doi: [10.1093/mnras/stad1557](https://doi.org/10.1093/mnras/stad1557)

Deng, Y., Li, H., Kannan, R., et al. 2024, MNRAS, 527, 478, doi: [10.1093/mnras/stad3202](https://doi.org/10.1093/mnras/stad3202)

Di Matteo, T., Springel, V., & Hernquist, L. 2005, Nature, 433, 604, doi: [10.1038/nature03335](https://doi.org/10.1038/nature03335)

Dolag, K., Sorce, J. G., Pilipenko, S., et al. 2023, Astrophysical Journal, 677, A169, doi: [10.1051/0004-6361/202346213](https://doi.org/10.1051/0004-6361/202346213)

Donahue, M., & Voit, G. M. 2022, PhR, 973, 1, doi: [10.1016/j.physrep.2022.04.005](https://doi.org/10.1016/j.physrep.2022.04.005)

Dubois, Y., Volonteri, M., Silk, J., et al. 2015, MNRAS, 452, 1502, doi: [10.1093/mnras/stv1416](https://doi.org/10.1093/mnras/stv1416)

Dutta, R., Sharma, P., Sarkar, K. C., & Stone, J. M. 2024, ApJ, 973, 148, doi: [10.3847/1538-4357/ad67d7](https://doi.org/10.3847/1538-4357/ad67d7)

El-Zant, A., Shlosman, I., & Hoffman, Y. 2001, ApJ, 560, 636, doi: [10.1086/322516](https://doi.org/10.1086/322516)

Fabian, A. C. 2012, ARA&A, 50, 455, doi: [10.1146/annurev-astro-081811-125521](https://doi.org/10.1146/annurev-astro-081811-125521)

Fahrion, K., Lyubenova, M., Hilker, M., et al. 2020, Astrophysical Journal, 637, A26, doi: [10.1051/0004-6361/202037685](https://doi.org/10.1051/0004-6361/202037685)

Ferrarese, L. 2002, ApJ, 578, 90, doi: [10.1086/342308](https://doi.org/10.1086/342308)

Fielding, D., Quataert, E., McCourt, M., & Thompson, T. A. 2017, MNRAS, 466, 3810, doi: [10.1093/mnras/stw3326](https://doi.org/10.1093/mnras/stw3326)

García-Bernete, I., Alonso-Herrero, A., Rigopoulou, D., et al. 2024, Astrophysical Journal, 681, L7, doi: [10.1051/0004-6361/202348266](https://doi.org/10.1051/0004-6361/202348266)

Gaspari, M., Eckert, D., Ettori, S., et al. 2019, ApJ, 884, 169, doi: [10.3847/1538-4357/ab3c5d](https://doi.org/10.3847/1538-4357/ab3c5d)

Genel, S., Vogelsberger, M., Springel, V., et al. 2014, MNRAS, 445, 175, doi: [10.1093/mnras/stu1654](https://doi.org/10.1093/mnras/stu1654)

Graham, A. W., & Sahu, N. 2023a, MNRAS, 518, 2177, doi: [10.1093/mnras/stac2019](https://doi.org/10.1093/mnras/stac2019)

—. 2023b, MNRAS, 520, 1975, doi: [10.1093/mnras/stad087](https://doi.org/10.1093/mnras/stad087)

Greene, J. E., Strader, J., & Ho, L. C. 2020, ARA&A, 58, 257, doi: [10.1146/annurev-astro-032620-021835](https://doi.org/10.1146/annurev-astro-032620-021835)

Habouzit, M., Volonteri, M., & Dubois, Y. 2017, MNRAS, 468, 3935, doi: [10.1093/mnras/stx666](https://doi.org/10.1093/mnras/stx666)

Habouzit, M., Li, Y., Somerville, R. S., et al. 2021, MNRAS, 503, 1940, doi: [10.1093/mnras/stab496](https://doi.org/10.1093/mnras/stab496)

Hearin, A. P., Zentner, A. R., van den Bosch, F. C., Campbell, D., & Tollerud, E. 2016, MNRAS, 460, 2552, doi: [10.1093/mnras/stw840](https://doi.org/10.1093/mnras/stw840)

Heckman, T. M., & Best, P. N. 2014, ARA&A, 52, 589, doi: [10.1146/annurev-astro-081913-035722](https://doi.org/10.1146/annurev-astro-081913-035722)

Henriques, B. M. B., White, S. D. M., Thomas, P. A., et al. 2015, MNRAS, 451, 2663, doi: [10.1093/mnras/stv705](https://doi.org/10.1093/mnras/stv705)

Hernquist, L., & Springel, V. 2003, MNRAS, 341, 1253, doi: [10.1046/j.1365-8711.2003.06499.x](https://doi.org/10.1046/j.1365-8711.2003.06499.x)

Hirano, S., & Yoshida, N. 2024, ApJ, 963, 2, doi: [10.3847/1538-4357/ad22e0](https://doi.org/10.3847/1538-4357/ad22e0)

Hong, H., Wang, H., Mo, H. J., et al. 2023, ApJ, 954, 183, doi: [10.3847/1538-4357/ace96f](https://doi.org/10.3847/1538-4357/ace96f)

Hopkins, P. F., Grudić, M. Y., Wetzel, A., et al. 2020, MNRAS, 491, 3702, doi: [10.1093/mnras/stz3129](https://doi.org/10.1093/mnras/stz3129)

Hopkins, P. F., Kereš, D., Oñorbe, J., et al. 2014, MNRAS, 445, 581, doi: [10.1093/mnras/stu1738](https://doi.org/10.1093/mnras/stu1738)

Hopkins, P. F., Quataert, E., & Murray, N. 2012, MNRAS, 421, 3522, doi: [10.1111/j.1365-2966.2012.20593.x](https://doi.org/10.1111/j.1365-2966.2012.20593.x)

Hopkins, P. F., Wellons, S., Angles-Alcazar, D., Faucher-Giguere, C.-A., & Grudic, M. Y. 2021, MNRAS, 510, 630, doi: [10.1093/mnras/stab3458](https://doi.org/10.1093/mnras/stab3458)

Hopkins, P. F., Wetzel, A., Kereš, D., et al. 2018, MNRAS, 480, 800, doi: [10.1093/mnras/sty1690](https://doi.org/10.1093/mnras/sty1690)

Hopkins, P. F., Squire, J., Su, K.-Y., et al. 2024, The Open Journal of Astrophysics, 7, 19, doi: [10.21105/astro.2310.04506](https://doi.org/10.21105/astro.2310.04506)

Jing, T., & Li, C. 2024, On the Origin of Quenched but Gas-rich Regions at Kiloparsec Scales in Nearby Galaxies, doi: [10.48550/arXiv.2408.12348](https://doi.org/10.48550/arXiv.2408.12348)

Kang, X., van den Bosch, F. C., Yang, X., et al. 2007, Monthly Notices of the Royal Astronomical Society, 378, 1531, doi: [10.1111/j.1365-2966.2007.11902.x](https://doi.org/10.1111/j.1365-2966.2007.11902.x)

Karam, J., & Sills, A. 2024, Dynamics of Star Cluster Formation: Mergers in Gas Rich Environments, arXiv, doi: [10.48550/arXiv.2404.06348](https://doi.org/10.48550/arXiv.2404.06348)

Karp, J. S. M., Lange, J. U., & Wechsler, R. H. 2023, The Astrophysical Journal, 949, L13, doi: [10.3847/2041-8213/acd3e9](https://doi.org/10.3847/2041-8213/acd3e9)

Kauffmann, G., & Charlot, S. 1998, MNRAS, 294, 705, doi: [10.1046/j.1365-8711.1998.01322.x](https://doi.org/10.1046/j.1365-8711.1998.01322.x)

Kauffmann, G., Li, C., Zhang, W., & Weinmann, S. 2013, MNRAS, 430, 1447, doi: [10.1093/mnras/stt007](https://doi.org/10.1093/mnras/stt007)

Kormendy, J., & Ho, L. C. 2013, ARA&A, 51, 511, doi: [10.1146/annurev-astro-082708-101811](https://doi.org/10.1146/annurev-astro-082708-101811)

Kubo, M., Umehata, H., Matsuda, Y., et al. 2022, ApJ, 935, 89, doi: [10.3847/1538-4357/ac7f2d](https://doi.org/10.3847/1538-4357/ac7f2d)

Kuhn, V., Guo, Y., Martin, A., et al. 2024, ApJL, 968, L15, doi: [10.3847/2041-8213/ad43eb](https://doi.org/10.3847/2041-8213/ad43eb)

Lagos, C. d. P., Stevens, A. R. H., Bower, R. G., et al. 2018, MNRAS, 473, 4956, doi: [10.1093/mnras/stx2667](https://doi.org/10.1093/mnras/stx2667)

Latif, M. A., Whalen, D., & Khochfar, S. 2022a, ApJ, 925, 28, doi: [10.3847/1538-4357/ac3916](https://doi.org/10.3847/1538-4357/ac3916)

Latif, M. A., Whalen, D. J., Khochfar, S., Herrington, N. P., & Woods, T. E. 2022b, Nature, 607, 48, doi: [10.1038/s41586-022-04813-y](https://doi.org/10.1038/s41586-022-04813-y)

Li, C., Kauffmann, G., Jing, Y. P., et al. 2006, MNRAS, 368, 21, doi: [10.1111/j.1365-2966.2006.10066.x](https://doi.org/10.1111/j.1365-2966.2006.10066.x)

Li, H., Vogelsberger, M., Marinacci, F., Sales, L. V., & Torrey, P. 2020, MNRAS, 499, 5862, doi: [10.1093/mnras/staa3122](https://doi.org/10.1093/mnras/staa3122)

Li, Q., Kilbinger, M., Luo, W., et al. 2024a, ApJL, 969, L25, doi: [10.3847/2041-8213/ad58b0](https://doi.org/10.3847/2041-8213/ad58b0)

Li, R., Wang, H., Mo, H. J., et al. 2022, ApJ, 936, 11, doi: [10.3847/1538-4357/ac8359](https://doi.org/10.3847/1538-4357/ac8359)

Li, Z., Inayoshi, K., Chen, K., Ichikawa, K., & Ho, L. C. 2024b, Little Red Dots: Rapidly Growing Black Holes Reddened by Extended Dusty Flows, doi: [10.48550/arXiv.2407.10760](https://doi.org/10.48550/arXiv.2407.10760)

Liang, J., Jiang, F., Mo, H., et al. 2024, Connection between Galaxy Morphology and Dark-Matter Halo Structure I: A Running Threshold for Thin Discs and Size Predictors from the Dark Sector, doi: [10.48550/arXiv.2403.14749](https://doi.org/10.48550/arXiv.2403.14749)

Lin, L., Hsieh, B.-C., Pan, H.-A., et al. 2019, ApJ, 872, 50, doi: [10.3847/1538-4357/aafa84](https://doi.org/10.3847/1538-4357/aafa84)

Liu, G., Zakamska, N. L., Greene, J. E., Nesvadba, N. P. H., & Liu, X. 2013, MNRAS, 436, 2576, doi: [10.1093/mnras/stt1755](https://doi.org/10.1093/mnras/stt1755)

Liu, W., Sun, M., Voit, G. M., et al. 2024, X-Ray Cool Core Remnants Heated by Strong Radio AGN Feedback, arXiv. <http://arxiv.org/abs/2405.09738>

Luo, X., Wang, H., Cui, W., et al. 2024, ApJ, 966, 236, doi: [10.3847/1538-4357/ad392e](https://doi.org/10.3847/1538-4357/ad392e)

Ma, X., Hopkins, P. F., Garrison-Kimmel, S., et al. 2018, MNRAS, 478, 1694, doi: [10.1093/mnras/sty1024](https://doi.org/10.1093/mnras/sty1024)

Maiolino, R., Scholtz, J., Witstok, J., et al. 2024, Nature, 627, 59, doi: [10.1038/s41586-024-07052-5](https://doi.org/10.1038/s41586-024-07052-5)

Marinacci, F., Vogelsberger, M., Pakmor, R., et al. 2018, MNRAS, 480, 5113, doi: [10.1093/mnras/sty2206](https://doi.org/10.1093/mnras/sty2206)

Martín-Navarro, I., Pillepich, A., Nelson, D., et al. 2021, *Nature*, 594, 187, doi: [10.1038/s41586-021-03545-9](https://doi.org/10.1038/s41586-021-03545-9)

Matthee, J., Naidu, R. P., Brammer, G., et al. 2024, *ApJ*, 963, 129, doi: [10.3847/1538-4357/ad2345](https://doi.org/10.3847/1538-4357/ad2345)

McAlpine, S., Bower, R. G., Harrison, C. M., et al. 2017, *MNRAS*, 468, 3395, doi: [10.1093/mnras/stx658](https://doi.org/10.1093/mnras/stx658)

McAlpine, S., Bower, R. G., Rosario, D. J., et al. 2018, *MNRAS*, 481, 3118, doi: [10.1093/mnras/sty2489](https://doi.org/10.1093/mnras/sty2489)

Mo, H., Chen, Y., & Wang, H. 2024, *MNRAS*, 532, 3808, doi: [10.1093/mnras/stae1727](https://doi.org/10.1093/mnras/stae1727)

Mo, H., van den Bosch, F., & White, S. 2010, *Galaxy Formation and Evolution* (Cambridge University Press, Cambridge)

Mo, H. J., & Mao, S. 2004, *MNRAS*, 353, 829, doi: [10.1111/j.1365-2966.2004.08114.x](https://doi.org/10.1111/j.1365-2966.2004.08114.x)

Mo, H. J., Mao, S., & White, S. D. M. 1998, *MNRAS*, 295, 319, doi: [10.1046/j.1365-8711.1998.01227.x](https://doi.org/10.1046/j.1365-8711.1998.01227.x)

Moster, B. P., Somerville, R. S., Maulbetsch, C., et al. 2010, *ApJ*, 710, 903, doi: [10.1088/0004-637X/710/2/903](https://doi.org/10.1088/0004-637X/710/2/903)

Mowla, L., Iyer, K., Asada, Y., et al. 2024, *The Firefly Sparkle: The Earliest Stages of the Assembly of A Milky Way-type Galaxy in a 600 Myr Old Universe*, doi: [10.48550/arXiv.2402.08696](https://doi.org/10.48550/arXiv.2402.08696)

Naiman, J. P., Pillepich, A., Springel, V., et al. 2018, *MNRAS*, 477, 1206, doi: [10.1093/mnras/sty618](https://doi.org/10.1093/mnras/sty618)

Nelson, D., Pillepich, A., Springel, V., et al. 2018, *MNRAS*, 475, 624, doi: [10.1093/mnras/stx3040](https://doi.org/10.1093/mnras/stx3040)

Nelson, D., Springel, V., Pillepich, A., et al. 2019, *Computational Astrophysics and Cosmology*, 6, 2, doi: [10.1186/s40668-019-0028-x](https://doi.org/10.1186/s40668-019-0028-x)

Padmanabhan, H., & Loeb, A. 2023, *ApJL*, 958, L7, doi: [10.3847/2041-8213/ad09ac](https://doi.org/10.3847/2041-8213/ad09ac)

Peebles, P. J. E. 1980, *The Large-Scale Structure of the Universe* (Princeton University Press)

Peng, C. Y. 2007, *ApJ*, 671, 1098, doi: [10.1086/522774](https://doi.org/10.1086/522774)

Pérez-González, P. G., Barro, G., Rieke, G. H., et al. 2024, *What Is the Nature of Little Red Dots and What Is Not, MIRI SMILES Edition*, doi: [10.48550/arXiv.2401.08782](https://doi.org/10.48550/arXiv.2401.08782)

Peschken, N., Lokas, E. L., & Athanassoula, E. 2020, *MNRAS*, 493, 1375, doi: [10.1093/mnras/staa299](https://doi.org/10.1093/mnras/staa299)

Pillepich, A., Nelson, D., Hernquist, L., et al. 2018a, *MNRAS*, 475, 648, doi: [10.1093/mnras/stx3112](https://doi.org/10.1093/mnras/stx3112)

Pillepich, A., Springel, V., Nelson, D., et al. 2018b, *MNRAS*, 473, 4077, doi: [10.1093/mnras/stx2656](https://doi.org/10.1093/mnras/stx2656)

Planck Collaboration, Ade, P. A. R., Aghanim, N., et al. 2016, *Astrophysical Journal*, 594, A13, doi: [10.1051/0004-6361/201525830](https://doi.org/10.1051/0004-6361/201525830)

Regan, J., & Volonteri, M. 2024, *Massive Black Hole Seeds*, arXiv, doi: [10.48550/arXiv.2405.17975](https://doi.org/10.48550/arXiv.2405.17975)

Rodriguez-Gomez, V., Genel, S., Vogelsberger, M., et al. 2015, *MNRAS*, 449, 49, doi: [10.1093/mnras/stv264](https://doi.org/10.1093/mnras/stv264)

Rodriguez-Gomez, V., Pillepich, A., Sales, L. V., et al. 2016, *Monthly Notices of the Royal Astronomical Society*, 458, 2371, doi: [10.1093/mnras/stw456](https://doi.org/10.1093/mnras/stw456)

Sawala, T., Frenk, C., Jasche, J., Johansson, P. H., & Lavaux, G. 2024, *Nature Astronomy*, 8, 247, doi: [10.1038/s41550-023-02130-6](https://doi.org/10.1038/s41550-023-02130-6)

Saxena, A., Overzier, R. A., Villar-Martín, M., et al. 2024, *MNRAS*, 531, 4391, doi: [10.1093/mnras/stae1406](https://doi.org/10.1093/mnras/stae1406)

Schaye, J., Vecchia, C. D., Booth, C. M., et al. 2010, *MNRAS*, 402, 1536, doi: [10.1111/j.1365-2966.2009.16029.x](https://doi.org/10.1111/j.1365-2966.2009.16029.x)

Schaye, J., Crain, R. A., Bower, R. G., et al. 2015, *MNRAS*, 446, 521, doi: [10.1093/mnras/stu2058](https://doi.org/10.1093/mnras/stu2058)

Shankar, F., Allevato, V., Bernardi, M., et al. 2020, *Nature Astronomy*, 4, 282, doi: [10.1038/s41550-019-0949-y](https://doi.org/10.1038/s41550-019-0949-y)

Sharma, M., & Theuns, T. 2020, *MNRAS*, 492, 2418, doi: [10.1093/mnras/stz2909](https://doi.org/10.1093/mnras/stz2909)

Shi, J., Peng, Y., Diemer, B., et al. 2022, *ApJ*, 927, 189, doi: [10.3847/1538-4357/ac51d5](https://doi.org/10.3847/1538-4357/ac51d5)

Shi, Y., Kremer, K., Grudić, M. Y., Gerling-Dunsmore, H. J., & Hopkins, P. F. 2023, *MNRAS*, 518, 3606, doi: [10.1093/mnras/stac3245](https://doi.org/10.1093/mnras/stac3245)

Sijacki, D., Vogelsberger, M., Genel, S., et al. 2015, *MNRAS*, 452, 575, doi: [10.1093/mnras/stv1340](https://doi.org/10.1093/mnras/stv1340)

Sivasankaran, A., Blecha, L., Torrey, P., et al. 2025, *MNRAS*, 537, 817, doi: [10.1093/mnras/staf062](https://doi.org/10.1093/mnras/staf062)

Sohn, J., Geller, M. J., Diaferio, A., & Rines, K. J. 2020, *ApJ*, 891, 129, doi: [10.3847/1538-4357/ab6e6a](https://doi.org/10.3847/1538-4357/ab6e6a)

Somerville, R. S., Hopkins, P. F., Cox, T. J., Robertson, B. E., & Hernquist, L. 2008, *MNRAS*, 391, 481, doi: [10.1111/j.1365-2966.2008.13805.x](https://doi.org/10.1111/j.1365-2966.2008.13805.x)

Spinoso, D., Bonoli, S., Valiante, R., Schneider, R., & Izquierdo-Villalba, D. 2023, *MNRAS*, 518, 4672, doi: [10.1093/mnras/stac3169](https://doi.org/10.1093/mnras/stac3169)

Springel, V., & Hernquist, L. 2003, *MNRAS*, 339, 289, doi: [10.1046/j.1365-8711.2003.06206.x](https://doi.org/10.1046/j.1365-8711.2003.06206.x)

Springel, V., White, S. D. M., Tormen, G., & Kauffmann, G. 2001, *MNRAS*, 328, 726, doi: [10.1046/j.1365-8711.2001.04912.x](https://doi.org/10.1046/j.1365-8711.2001.04912.x)

Springel, V., Pakmor, R., Pillepich, A., et al. 2018, *MNRAS*, 475, 676, doi: [10.1093/mnras/stx3304](https://doi.org/10.1093/mnras/stx3304)

Stacy, A., Bromm, V., & Lee, A. T. 2016, *MNRAS*, 462, 1307, doi: [10.1093/mnras/stw1728](https://doi.org/10.1093/mnras/stw1728)

Terrazas, B. A., Bell, E. F., Pillepich, A., et al. 2020, *MNRAS*, 493, 1888, doi: [10.1093/mnras/staa374](https://doi.org/10.1093/mnras/staa374)

Tully, R. B., Pomarède, D., Graziani, R., et al. 2019, *ApJ*, 880, 24, doi: [10.3847/1538-4357/ab2597](https://doi.org/10.3847/1538-4357/ab2597)

Ventura, E. M., Qin, Y., Balu, S., & Wyithe, J. S. B. 2024, Semi-Analytic Modelling of Pop. III Star Formation and Metallicity Evolution – I. Impact on the UV Luminosity Functions at  $z = 9\text{--}16$ , arXiv, doi: [10.48550/arXiv.2401.07396](https://doi.org/10.48550/arXiv.2401.07396)

Vogelsberger, M., Genel, S., Sijacki, D., et al. 2013, MNRAS, 436, 3031, doi: [10.1093/mnras/stt1789](https://doi.org/10.1093/mnras/stt1789)

Voit, G. M., Oppenheimer, B. D., Bell, E. F., Terrazas, B., & Donahue, M. 2024, ApJ, 960, 28, doi: [10.3847/1538-4357/ad0039](https://doi.org/10.3847/1538-4357/ad0039)

Wang, H., Mo, H. J., Yang, X., et al. 2016, ApJ, 831, 164, doi: [10.3847/0004-637X/831/2/164](https://doi.org/10.3847/0004-637X/831/2/164)

Wang, K., Peng, Y., & Chen, Y. 2023, MNRAS, 523, 1268, doi: [10.1093/mnras/stad1169](https://doi.org/10.1093/mnras/stad1169)

Wang, T., Sun, H., Zhou, L., et al. 2024a, The True Number Density of Massive Galaxies in the Early Universe Revealed by JWST/MIRI

Wang, X., Cheng, C., Ge, J., et al. 2024b, ApJ, 967, L42, doi: [10.3847/2041-8213/ad4ced](https://doi.org/10.3847/2041-8213/ad4ced)

Wang, Y., Yang, X., Gu, Y., et al. 2024c, ApJ, 971, 119, doi: [10.3847/1538-4357/ad5294](https://doi.org/10.3847/1538-4357/ad5294)

Wechsler, R. H., & Tinker, J. L. 2018, ARA&A, 56, 435, doi: [10.1146/annurev-astro-081817-051756](https://doi.org/10.1146/annurev-astro-081817-051756)

Weinberger, R., Springel, V., Hernquist, L., et al. 2017, MNRAS, 465, 3291, doi: [10.1093/mnras/stw2944](https://doi.org/10.1093/mnras/stw2944)

Weinberger, R., Springel, V., Pakmor, R., et al. 2018, MNRAS, 479, 4056, doi: [10.1093/mnras/sty1733](https://doi.org/10.1093/mnras/sty1733)

White, S. D. M., & Rees, M. J. 1978, MNRAS, 183, 341, doi: [10.1093/mnras/183.3.341](https://doi.org/10.1093/mnras/183.3.341)

Wise, J. H., Regan, J. A., O’Shea, B. W., et al. 2019, Nature, 566, 85, doi: [10.1038/s41586-019-0873-4](https://doi.org/10.1038/s41586-019-0873-4)

Xu, H., Zheng, Z., Guo, H., et al. 2018, MNRAS, 481, 5470, doi: [10.1093/mnras/sty2615](https://doi.org/10.1093/mnras/sty2615)

Yang, M., Zhu, L., Lei, Y., et al. 2024, MNRAS, 528, 5295, doi: [10.1093/mnras/stae335](https://doi.org/10.1093/mnras/stae335)

Yang, X., Mo, H. J., & van den Bosch, F. C. 2003, MNRAS, 339, 1057, doi: [10.1046/j.1365-8711.2003.06254.x](https://doi.org/10.1046/j.1365-8711.2003.06254.x)

—. 2008, ApJ, 676, 248, doi: [10.1086/528954](https://doi.org/10.1086/528954)

—. 2009, ApJ, 695, 900, doi: [10.1088/0004-637X/695/2/900](https://doi.org/10.1088/0004-637X/695/2/900)

Yang, X., Mo, H. J., van den Bosch, F. C., et al. 2007, ApJ, 671, 153, doi: [10.1086/522027](https://doi.org/10.1086/522027)

Yang, X., Mo, H. J., van den Bosch, F. C., Zhang, Y., & Han, J. 2012, ApJ, 752, 41, doi: [10.1088/0004-637X/752/1/41](https://doi.org/10.1088/0004-637X/752/1/41)

Yu, S., Bullock, J. S., Gurvich, A. B., et al. 2023, MNRAS, 523, 6220, doi: [10.1093/mnras/stad1806](https://doi.org/10.1093/mnras/stad1806)

Zahid, H. J., Geller, M. J., Fabricant, D. G., & Hwang, H. S. 2016, ApJ, 832, 203, doi: [10.3847/0004-637X/832/2/203](https://doi.org/10.3847/0004-637X/832/2/203)

Zahid, H. J., Sohn, J., & Geller, M. J. 2018, ApJ, 859, 96, doi: [10.3847/1538-4357/aae31](https://doi.org/10.3847/1538-4357/aae31)

Zhang, Z., Wang, H., Luo, W., et al. 2024, ApJ, 960, 71, doi: [10.3847/1538-4357/ad0892](https://doi.org/10.3847/1538-4357/ad0892)

—. 2022, Astrophysical Journal, 663, A85, doi: [10.1051/0004-6361/202142866](https://doi.org/10.1051/0004-6361/202142866)

Zhao, D. H., Mo, H. J., Jing, Y. P., & Börner, G. 2003, MNRAS, 339, 12, doi: [10.1046/j.1365-8711.2003.06135.x](https://doi.org/10.1046/j.1365-8711.2003.06135.x)

Zheng, Z., Berlind, A. A., Weinberg, D. H., et al. 2005, ApJ, 633, 791, doi: [10.1086/466510](https://doi.org/10.1086/466510)

Zhu, L., van de Ven, G., Leaman, R., et al. 2020, MNRAS, 496, 1579, doi: [10.1093/mnras/staa1584](https://doi.org/10.1093/mnras/staa1584)

Zhu, L., Pillepich, A., van de Ven, G., et al. 2022, Astrophysical Journal, 660, A20, doi: [10.1051/0004-6361/202142496](https://doi.org/10.1051/0004-6361/202142496)

Zhuang, M.-Y., & Ho, L. C. 2023, Nature Astronomy, doi: [10.1038/s41550-023-02051-4](https://doi.org/10.1038/s41550-023-02051-4)

Zinger, E., Pillepich, A., Nelson, D., et al. 2020, MNRAS, 499, 768, doi: [10.1093/mnras/staa2607](https://doi.org/10.1093/mnras/staa2607)